Physics of Fluids

RESEARCH ARTICLE | AUGUST 02 2023

How wavelength affects hydrodynamic performance of two accelerating mirror-symmetric undulating hydrofoils

Zhonglu Lin (林中路) ; Dongfang Liang (梁东方) ; Amneet Pal Singh Bhalla ; Ahmed A. Sheikh Al-Shabab ; Martin Skote ; Wei Zheng (郑炜) ; Yu Zhang (张宇)

Physics of Fluids 35, 081901 (2023)
https://doi.org/10.1063/5.0155661

Physics of Fluids ARTICLE pubs.aip.org/aip/pof

How wavelength affects hydrodynamic performance of two accelerating mirror-symmetric undulating hydrofoils

Cite as: Phys. Fluids **35**, 081901 (2023); doi: 10.1063/5.0155661
Submitted: 22 April 2023 · Accepted: 10 July 2023 ·
Published Online: 2 August 2023

Zhonglu Lin (林中路),[1,2,3] Dongfang Liang (梁东方),[2] Amneet Pal Singh Bhalla,[4] Ahmed A. Sheikh Al-Shabab,[5] Martin Skote,[5] Wei Zheng (郑炜),[1,3,6,7] and Yu Zhang (张宇)[1,3,a)]

AFFILIATIONS

[1]Key Laboratory of Underwater Acoustic Communication and Marine Information Technology of the Ministry of Education, College of Ocean and Earth Sciences, Xiamen University, Xiamen 361005, Fujian, China
[2]Engineering Department, University of Cambridge, Cambridge, Cambridgeshire CB2 1PZ, United Kingdom
[3]State Key Laboratory of Marine Environmental Science, College of Ocean and Earth Sciences, Xiamen University, Xiamen 361005, Fujian, China
[4]Department of Mechanical Engineering, San Diego State University, San Diego, California 92182-1323, USA
[5]School of Aerospace, Transport and Manufacturing, Cranfield University, Cranfield, Bedfordshire MK43 0AL, United Kingdom
[6]Pen-Tung Sah Institute of Micro-Nano Science and Technology, Xiamen University, Xiamen 361005, Fujian, China
[7]Discipline of Intelligent Instrument and Equipment, Xiamen University, Xiamen 361005, Fujian, China

[a)]**Author to whom correspondence should be addressed:** yuzhang@xmu.edu.cn

ABSTRACT

Fish schools are capable of simultaneous linear acceleration. To reveal the underlying hydrodynamic mechanism, we numerically investigate how Reynolds number $Re = 1000$–2000, Strouhal number $St = 0.2$–0.7, and wavelength $\lambda = 0.5$–2 affect the mean net thrust and net propulsive efficiency of two side-by-side hydrofoils undulating in anti-phase. In total, 550 cases are simulated using immersed boundary method. The thrust increases significantly with the wavelength and the Strouhal number, yet only slightly with the Reynolds number. We apply a symbolic regression algorithm to formulate this relationship. Furthermore, we find that mirror-symmetric schooling can achieve a net thrust more than ten times that of a single swimmer, especially at low Reynolds numbers. The highest efficiency is obtained at $St = 0.5$ and $\lambda = 1.2$, where St is consistent with that observed in the linear-accelerating natural swimmers, e.g., Crevalle jack. Six distinct flow structures are identified. The highest thrust corresponds to an asymmetric flow pattern, whereas the highest efficiency occurs when the flow is symmetric with converging vortex streets.

I. INTRODUCTION

A. Background overview

Fish swimming have been extensively studied for decades in various disciplines, e.g., morphology (Webb, 1984), animal behavior (Ashraf *et al.*, 2017), robotics (Li *et al.*, 2020), and especially hydrodynamics (Weihs, 1973; Borazjani and Sotiropoulos, 2010; Dong and Lu, 2007; Maertens *et al.*, 2015; Maertens *et al.*, 2017; Pan and Dong, 2020; Chao *et al.*, 2019; and Chao *et al.*, 2021). The investigation of fish swimming mechanisms can inspire the next-generation biomimetic design of autonomous underwater vehicles (AUVs), as the locomotive performance of commercially available AUVs is yet to match those of natural swimmers (Fish, 2020). The present research focuses on the effects of the wavelength on two undulating NACA0012 hydrofoils swimming side-by-side. The results can help understand the underlying mechanism of accelerated fish schools. Simultaneous acceleration of fish school can frequently occur in nature (Partridge, 1981) to evade predators (Zheng *et al.*, 2005; Deng and Liu, 2021) or to conduct collective maneuver (Lecheval *et al.*, 2018) using vision (Rosenthal *et al.*, 2015), lateral line (Coombs and Montgomery, 2014), and proprioceptive sensing (Li *et al.*, 2021a). Although the effects of the wavelength have been investigated in the context of a single swimmer (Thekkethil *et al.*, 2017; Khalid *et al.*, 2021; and Chao *et al.*, 2022), it remains an

open question as to how wavelength kinematics affect accelerating fish schools. The following reviews on fish swimming studies regarding the wavelength effect, acceleration, and side-by-side fish schooling highlight the research gap that can be filled by the present study.

In nature, the swimming body wavelength is not only different across various species with different swimming styles at steady swimming (Santo *et al.*, 2021) but also varies with the locomotion phase of a single swimmer (Du Clos *et al.*, 2019), e.g., starting from rest, linear acceleration, and steady swimming. Santo *et al.* (2021) recently conducted a comparative study on the kinematics of 44 body-caudal fin (BCF) fish species, focusing on the steady swimming phase. Santo *et al.* (2021) summarized and compared the wavelengths of different BCF species, considering the four classic swimming styles of *anguilliform*, *subcarangiform*, *carangiform*, and *thunniform*. The median wavelength significantly increased from *anguilliform* (0.75 body length) to *thunniform* (1.14 body length), yet the wavelength for the tested species occupies a broad range from 0.5 body length to 1.5 body length. For conciseness, we abbreviate "body length" as "BL" in the following content. The wavelength of four swimming styles overlaps from 0.75BL to 1.35BL, indicating this wavelength range may be compatible with swimmers of various body shapes and swimmers of different swimming styles. The results by Santo *et al.* (2021) have driven us to focus on a similar range of wavelengths, which will be presented later in Sec. II A. Du Clos *et al.* (2019) studied how an *anguilliform* swimmer accelerates from rest, and compared the kinematics during steady swimming and acceleration. They discovered that the wavelength during escape acceleration $\lambda \approx 2$, much longer than that during steady swimming with $\lambda = 0.8$. Nangia *et al.* (2017a) conducted a meta-analysis regarding the wavelength and the Strouhal number for various BCF species, finding a convergence of the ratio of the wavelength to the tail amplitude during undulation. Nangia *et al.* (2017a) utilized the ConstraintIB module of open-source immersed boundary software, IBAMR, which is also used in our present study.

B. Wavelength effects for a single swimmer during steady-swimming and linear acceleration

Many numerical studies focused on the wavelength effect of a single swimmer, both in 2 and 3D. Chao *et al.* (2022) recently conducted a thorough investigation of the hydrodynamic performance of a single slender swimmer with various Strouhal numbers $St = 0.1$–1, Reynolds numbers $Re = 50$–2000, and $\lambda = 0.5$–2, and they discovered seven types of wake structures. They were able to condense the simulation results into a few formulas. Their study has inspired the present study's choice of parametric space. Khalid *et al.* (2020) studied how a single tethered undulating 2D NACA0012 hydrofoil performs with either *anguilliform* or *carangiform* kinematics in a parametric sweep of $Re = 100, 1000, 5000$, $St = 0.1$–0.8, and $\lambda = 0.5$–1.5. They found that wavelengths do not necessarily optimize the hydrodynamic performance of natural swimmers. Thekkethil *et al.* (2017), Thekkethil *et al.* (2018, 2020), and Gupta *et al.* (2021) conducted a series of studies regarding how the wavelength affects the thrust and propulsive efficiency of a single undulating NACA0012 hydrofoil. Khalid *et al.* (2021) conducted high-fidelity 3D simulations of a steady-swimming American eel at $St = 0.3$–0.4, investigating the influences of wavelengths at $\lambda = 0.65$–1.25. They found that short wavelengths are more hydrodynamically advantageous for *anguilliform* swimmers during their steady motion. Borazjani and Sotiropoulos (2008, 2009) conducted a 3D simulation to study a steady-swimming *carangiform* (Borazjani and Sotiropoulos, 2008) and an *anguilliform* (Borazjani and Sotiropoulos, 2009) swimmer tethered in a free stream flow at $Re = 300$, 4000, whereas the wavelength is configured at $\lambda = 0.642$–1.1.

In addition, in the present paper, we apply 2D model rather than 3D considering computational cost to simulate 550 cases. Additionally, 2D simulation has proven to reveal fundamental patterns in undulating hydrofoils with various wavelengths in the laminar flow regime (Chao *et al.*, 2022).

The above-mentioned studies have focused on the steady swimming phase. However, steady swimming is a rare scenario for fish swimming. Other conditions include the starting from rest (Domenici and Hale, 2019) and the linear acceleration (Akanyeti *et al.*, 2017). The linear acceleration occurs when they travel or hold a position in a variable speed or turbulent flow Tytell (2004). While steady-swimming and fast-start (Eaton *et al.*, 1977; Tytell and Lauder, 2008; and Borazjani *et al.*, 2012; Borazjani, 2013) are relatively well studied, linear acceleration is still not well understood in both biological and hydrodynamic aspects for a single swimmer, let alone for fish schools.

Wavelength correlates significantly with acceleration and speed during the linear acceleration phase of fish swimming. The existing biological research almost all focused on a *single* accelerating fish. An overview of the wavelength and swimming styles is depicted in Fig. 1. Schwalbe *et al.* (2019) scrutinized the function of red muscle, i.e., slow-twitch muscle for sustained activities, during the acceleration of bluegill sunfish *Lepomis macrochirus* and how it affects the fish kinematics. They discovered that the fish's undulation kinematics during acceleration differs from that during steady swimming. Body wavelength decreases significantly during acceleration, yet increases significantly with swimming speed. Their research focused on the bluegill sunfish *Lepomis macrochirus*. At different acceleration levels, the fish body wavelength can range from 0.75BL to 0.9BL. They focused on the fish muscle activation and observation of kinematics. Akanyeti *et al.* (2017) conducted both biological and robotic fish experiments to investigate the kinematic characteristics and hydrodynamic performance during linear acceleration. Their investigation was carried out using a tethered robotic fish while varying the free stream flow to study the acceleration at consecutive instants. Our present problem setup is similar to their experimental configuration. They found that tail-beat frequency, rather than amplitude, is most effective on swimming speed and acceleration. The tail-beat amplitude remains constant during steady swimming or acceleration. Hence, our present study fixes tail-beat amplitude while varying the Strouhal number. Tytell (2004) conducted the first quantitative research on the linear acceleration of an *anguilliform* swimmer, focusing on its kinematics and wake hydrodynamics. They found that body wavelength λ and tail-beat frequency both significantly increase with steady swimming speed.

C. Side-by-side steady swimming with constant wavelength

Side-by-side fish schooling is relatively well studied, yet most studies have focused on the steady swimming scenario with a fixed wavelength. Ashraf *et al.* (2017) conducted a fish schooling experiment, discovering that fish favors the phalanx formation, i.e., side-by-side of multiple fish, at relatively high steady-swimming speed. The tested Reynolds number ranges from 1000 to 6000. Li *et al.* (2021b)

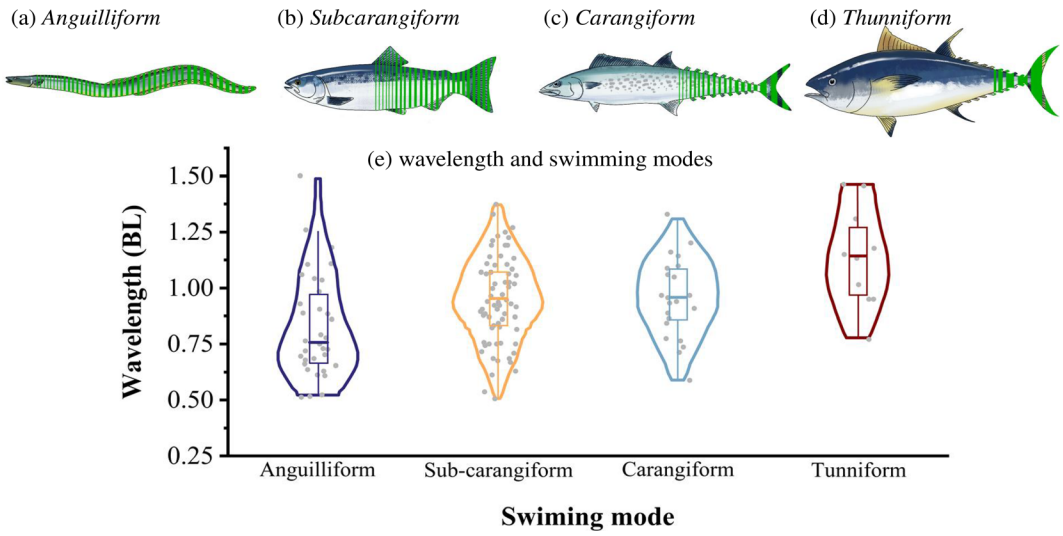

FIG. 1. Four different swimming modes of body-caudal-fin type locomotion (a) *Anguilliform* (body undulation, e.g., eel), (b) *Subcarangiform* (body undulation with caudal fin pitching, e.g., salmonid), (c) *Carangiform* (minor body undulation with caudal fin pitching, e.g., makrell), (d) *Thunniform* (mainly caudal fin pitching, e.g., tuna). The shaded area demonstrates the body parts with a significant lateral motion to generate thrust [redrawn from figures by Lindsey (1978) and Sfakiotakis *et al.* (1999)]. (d) distribution of wavelength with the four swimming modes [adapted from figure by Santo *et al.* (2021)]: These four types have wavelengths ranging from 0.5 to 2 body length for steady swimming conditions across various fish species regardless of the aforementioned body-caudal fin sub-types.

investigated the schooling of two robotic fish of *subcarangiform*, swimming steadily side-by-side with rigid linking between them, with the lateral distance fixed at 0.33BL. For schooling swimmers, they discovered maximum speed and efficiency at in-phase and anti-phase conditions, respectively, which are compared with a single swimmer. In the present paper, we also fix the gap distance at 0.33BL. For side-by-side and anti-phase pitching foils, previous studies reached a consensus that much higher thrust can be produced with efficiency similar to a single swimmer (Dewey *et al.*, 2014; Huera-Huarte, 2018; Gungor and Hemmati, 2021; and Yucel *et al.*, 2022). Our present paper further investigates the hydrodynamic effects due to various wavelengths. Li *et al.* (2020) conducted a thorough study on a tethered two-fish school at a steady swimming phase, combining robotic fish experiments and biological observation. They discovered that the front-back distance and phase difference most significantly affected schooling performance. The lateral distance varies from 0.27 to 0.33 in this study. Shrivastava *et al.* (2017) conducted a 2D simulation of three hydrofoils swimming side-by-side. Interaction between the swimmers can be observed at a lateral distance less than 1BL with $St = 0.4$–0.8, $A_{\max}$, $\lambda = 1$, $Re = 400$. Wei *et al.* (2022) simulated two initially side-by-side swimmers passively self-propelling with three degrees of freedom. They configured the initial gap ratio as $G = 0.4$–0.9 and observed improved schooling performance between the two swimmers. Therefore, the present lateral distance of 0.33BL should allow sufficient schooling interaction between the two swimmers. Gungor *et al.* (2022) investigated the unsteady hydrodynamics of two pitching foils in side-by-side formation. By drawing wake maps, they discovered three distinct vortex patterns of separated, merged, and transitional-merged wake.

D. Present study scope

In summary, the above-mentioned literature has inspired us that fish-body wavelength is a key factor affecting the fluid–structure interaction of fish-like swimmers, yet the research regarding the wavelength effect on schooling and accelerating swimmers is relatively scarce, despite its occurrence in the nature, e.g., fish school escaping from predator. Also, we use the term "mirror-symmetric" as an equivalent of "side-by-side and anti-phase," not only for the sake of conciseness but also because we would like to strengthen the physically interesting phenomenon of flow symmetry and its breaking at certain conditions. More specifically, although excellent studies have emerged to examine single fish wavelength effects (Santo *et al.*, 2021; Khalid *et al.*, 2021; Thekkethil *et al.*, 2020; Du Clos *et al.*, 2019; and Nangia *et al.*, 2017a), linear acceleration (Tytell, 2004; Akanyeti *et al.*, 2017; and Schwalbe *et al.*, 2019), and side-by-side schooling (Wei *et al.*, 2022; Li *et al.*, 2021b; Shrivastava *et al.*, 2017; and Ashraf *et al.*, 2017), how body wavelength affects the linear acceleration of two side-by-side fish-like swimmers has never been systematically investigated. We aim to present a thorough investigation in the present paper, which can be helpful in understanding the fish schooling behavior and to design the collective locomotion strategy of underwater fish-like AUVs. The rich physics in side-by-side fish schooling can also be relevant to the flow-mediated interaction between two oscillating cylinders (Lin *et al.*, 2023b, 2019, 2018a, 2018b, 2017, 2016; Gazzola *et al.*, 2012; Nair and Kanso, 2007; and Lamb, 1932).

II. METHODOLOGY

In this section, we present the methodology of the current study. Section II A describes the representative problem setup accounting for the schooling swimmers, including geometry, kinematic equation, and non-dimensional analysis. Section II B discusses the computational method to implement the problem setup.

A. Problem setup

It is not uncommon to observe simplified models relevant to fish swimming, including a traveling wavy boundary (Ma *et al.*, 2019;

Wang *et al.*, 2021), filaments (Ni *et al.*, 2023), and undulating NACA foils (Lin *et al.*, 2023a). The present problem setup applies NACA0012 hydrofoil to represent the fish-like swimmer, since the NACA foils have been extensively used as a representation in the previous investigations (Deng *et al.*, 2022, 2016, 2015; Shao *et al.*, 2010; Deng *et al.*, 2007; Yu and Huang, 2021; and Pan and Dong, 2022). The complete configuration is summarized in Fig. 2. The accelerated fish schooling problem is represented by a two-dimensional form with two wavy hydrofoils undulating side-by-side. The 2D configuration should adequately describe the present laminar flow regime with $Re \leq 2000$ (Gazzola *et al.*, 2014; Chao *et al.*, 2022).

The fish body is simplified as a 2D NACA0012 hydrofoil to describe bio-propulsion problems with pitching (Moriche *et al.*, 2016) and undulating hydrofoils (Thekkethil *et al.*, 2017). The geometry of a NACA0012 hydrofoil is similar to that of a *carangiform* or *subcarangiform* swimmer. The two foils are placed side-by-side while undulating in anti-phase to concentrate on a limited number of variables typical for fish schooling (Ashraf *et al.*, 2017). The kinematics of the swimmers is described by the traveling wave equations in the non-dimensional form

$$Y_1 = A_{\max} X_1 \sin\left[2\pi\left(\frac{X_1}{\lambda} - \frac{St}{2A_{\max}}t\right)\right], \tag{1}$$

$$Y_2 = A_{\max} X_2 \sin\left[2\pi\left(\frac{X_2}{\lambda} - \frac{St}{2A_{\max}}t\right) + \pi\right]. \tag{2}$$

This is also a common configuration (Thekkethil *et al.*, 2018) and is chosen here for the convenience of comparison. For completeness, the meaning of the variables is listed as follows: $Y_i = Y'_i/C'$ is the center-line lateral displacement of each hydrofoil; $X_i = X'_i/C'$ is the streamwise position on the centerline; and $i = 1$ denotes the top swimmer, while $i = 2$ represents the bottom swimmer. $t = t'u'_\infty/C'$ is non-dimensional time; u'_∞ is the free-stream velocity; $A_{\max} = A'_{\max}/C'$ is non-dimensional tail tip amplitude, where C' is the fish body length; $a_{\max}$ is the dimensional tail-amplitude; $\lambda = \lambda'/C'$ is non-dimensional wavelength, with λ' being the dimensional foil undulating wavelength; $St = 2f'A'_{\max}/u'_\infty$ is the Strouhal number, with f' being the dimensional undulating frequency. Here, dashed alphabets denote dimensional parameters.

In addition, non-dimensional groups to describe a particular case are listed in Table I together with the investigated parametric space, in

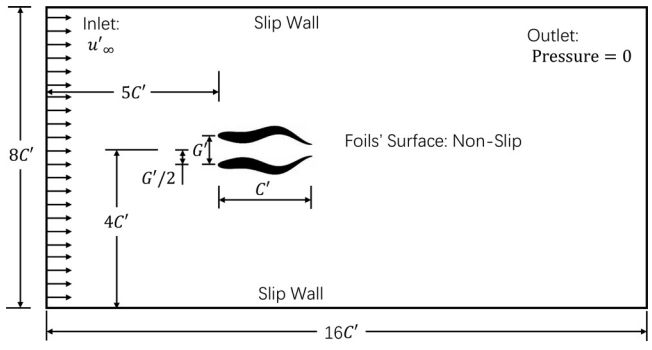

FIG. 2. Sketch of the present problem setup: two side-by-side fish swimming in anti-phase with a fixed lateral gap distance $G = 0.33$. The two swimmers are mirror symmetric to each other along the horizontal line $y = 4C$.

TABLE I. Non-dimensional input parameters and the involved range of value.

Reynolds number	Re	$\rho' u'_\infty C'/\mu'$	$1000 - 2000$
Strouhal number	St	$2f'A'_{\max}/u'_\infty$	$0.2 - 0.7$
Wavelength	λ	λ'/C'	$0.5 - 2$

which ρ' is the fluid density; f' is the undulating frequency; and μ' is the dynamic viscosity. The non-dimensional lateral and front-back distances are fixed at $G = G'/C' = 0.33$ and $D = D'/C' = 0$. In summary, only three variables are involved in the present study: the Reynolds number $Re = 1000$–2000, the Strouhal number $St = 0.2$–0.7, and non-dimensional wavelength $\lambda = 0.5$–2.0.

The outputted metrics of the swimming performance are listed in Table II. Thrust is directly relevant to acceleration, whereas net propulsive efficiency measures how efficiently the input energy is converted to the net thrust for acceleration. The examination of the vorticity field is necessary to examine the flow symmetry and stealth capacity. In Table II, $F_{T,i}$ is the net thrust on hydrofoils; $C_{L,i}$ is the instantaneous lateral force coefficient; $\boldsymbol{u}$ is the fluid velocity. ω^* is the non-dimensional vorticity, whereas P^* stands for the non-dimensional pressure.

B. Simulation method

The present paper simulates the problem using a customized version of the ConstraintIB module (Bhalla *et al.*, 2013; Griffith and Patankar, 2020) implemented in IBAMR (Griffith, 2013), which is an open-source immersed boundary method simulation software that depends on several underlying advanced libraries including SAMRAI (Hornung and Kohn, 2002; Hornung *et al.*, 2006), PETSc (Balay *et al.*, 1997, 2023a, 2023b), hypre (Falgout *et al.*, 2010; Balay *et al.*, 1997), and libmesh (Kirk *et al.*, 2006). It is chosen for its adaptive mesh refinement capacity of the Eulerian background mesh, allowing both computational efficiency and adequate accuracy. The ConstraintIB method has been extensively validated (Bhalla *et al.*, 2013; Bhalla *et al.*, 2013; Bhalla *et al.*, 2014; Nangia *et al.*, 2017b; Nangia *et al.*, 2019; Griffith and Patankar, 2020; and Bhalla *et al.*, 2020). The present customized version has also been validated in Lin *et al.* (2023a). The maximum Reynolds number $Re \leq 2000$ in the present study is lower than that in a previous study (Lin *et al.*, 2023a) with $Re = 5000$, so here we adopt the same mesh refinement and time step setting that has been verified for mesh independence. Each numerical simulation was run for 20 cycles of undulation.

TABLE II. Non-dimensional output parameters for swimming performance.

Cycle-averaged net thrust coefficient	$\bar{C}_{T,i}$	$\frac{1}{T}\int_t^{t+T} C_T \mathrm{d}t = \frac{1}{T}\int_t^{t+T} 2F_{T,i}/\rho u_\infty^2 C \mathrm{d}t$
Net propulsive efficiency	η_i	$P_{\text{out},i}/P_{\text{in},i} = \bar{C}_T/\bar{C}_P$
Fluid vorticity	$\boldsymbol{\omega}^*$	$\nabla \times \boldsymbol{u}$
Fluid pressure	$\boldsymbol{P}^*$	$p/\rho u_\infty$

C. Symbolic regression method

The open-source symbolic regression library, PySR (Cranmer, 2023), is utilized to automatically extract the interpretable symbolic models for net thrust force, i.e., Eq. (3), from the data accumulated from the 550 simulated cases. It is based on multi-population evolutionary algorithm with a special evolve–simplify–optimize cycle, being capable to high efficiency parallel computation with integration to deep learning tools. PySR has been proven useful in many studies, including cloud cover formation (Grundner *et al.*, 2023), electron transfer rules (Li *et al.*, 2023), and discovering astrophysical relations (Matchev *et al.*, 2022). The present study chose PySR for the customizable configuration that is capable of reducing the regression time, and for the parallelization that speeds up the data-discovery speed.

III. RESULTS AND DISCUSSION

In this section, we present and discuss our discoveries from 550 cases regarding two side-by-side and anti-phase wavy NACA0012 hydrofoils in the parametric space of the Reynolds number $Re = 1000$–2000, the Strouhal number $St = 0.2$–0.7, and the wavelength $\lambda = 0.5$–2. Section III A discusses how St, λ, and Re influence the net thrust $\bar{C}_{T,pair}$ for each swimmer by drawing heat maps while generating a formula for a high-level summary. We also compare the simulated schooling thrust with the analytical formula describing thrust by a single swimmer (Chao *et al.*, 2022) finding interesting results. Section III B presents the dependence of net propulsive efficiency on St, λ, and Re, with extra focus on the cases with the highest efficiency. In Sec. III C, we classify observed flow structures into several types, while connecting them to high-thrust or high-efficiency regimes.

A. How St, λ, and Re affect net thrust $\bar{C}_{T,pair}$

This subsection discusses how net propulsive efficiency varies with the Reynolds number $Re = 1000$–2000, the Strouhal number $St = 0.2$–0.7, and the wavelength $\lambda = 0.5$–2. The thrust generally increases with the Strouhal number and the wavelength, whereas the effect of the Reynolds number is marginal, as demonstrated in Fig. 3. The contour line of $\bar{C}_{T,pair} = 0$ at the white region denotes the steady swimming state, which is often discussed in numerical (Borazjani and Sotiropoulos, 2008) and experimental (Li *et al.*, 2020) studies of fish

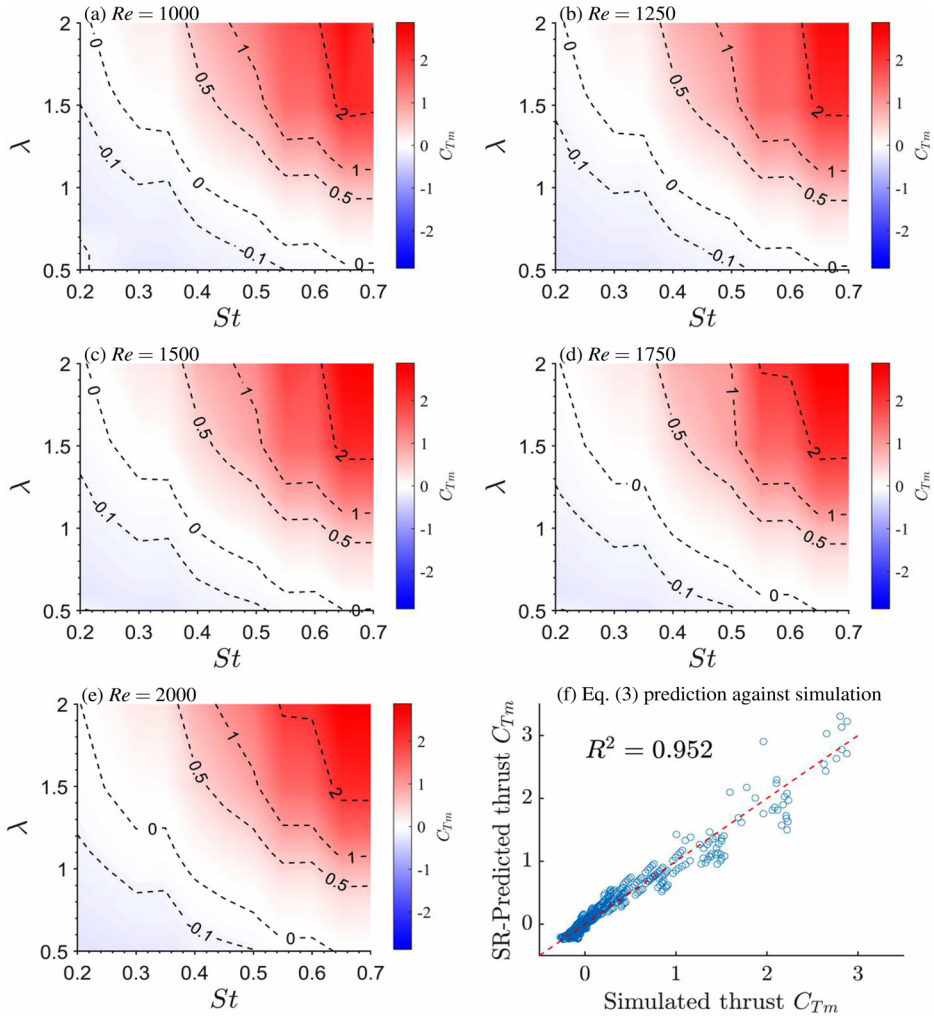

FIG. 3. Heat map for mean net thrust $\bar{C}_{T,pair}$ at the Strouhal number $St = 0.2 - 0.7$, the wavelength $\lambda = 0.5 - 2$, and the Reynolds numbers at (a) $Re = 1000$, (b) $Re = 1250$, (c) $Re = 1500$, (d) $Re = 1750$, and (e) $Re = 2000$. (f) Symbolic regression prediction accuracy comparing simulation results and Eq. (3). The thrust on two swimmers is identical due to the symmetrical situation. The positive thrust, i.e., forward acceleration, is indicated by the positive values with red color. Conversely, the negative thrust, i.e., deceleration, is indicated by the negative values with blue color. The contour line of $\bar{C}_{T,pair} = 0$ represents the zero net thrust scenarios, i.e., steady swimming state. Only marginal differences can be observed across various Reynolds numbers.

swimming. With a higher St or λ, the thrust becomes positive $\bar{C}_{\mathrm{T,pair}} > 0$, i.e., the hydrofoil school is accelerating. Conversely, with a lower St or λ, the foils are decelerating with negative thrust. Re only slightly affects this overall trend. This pattern corresponds well with the single swimmer scenario discussed in Chao *et al.* (2022), where the effect of Re on net thrust becomes insignificant at $Re > 1000$, while a positive correlation exists between net thrust and wavelength/Strouhal number. Here, the representative net thrust is calculated as the average value for the two swimmers, i.e., $\bar{C}_{\mathrm{T,pair}} = (\bar{C}_{\mathrm{T},1} + \bar{C}_{\mathrm{T},2})/2$, where $\bar{C}_{\mathrm{T,pair}} = \bar{C}_{\mathrm{T},1} = \bar{C}_{\mathrm{T},2}$ establishes for the symmetrical cases. $\bar{C}_{\mathrm{T},i}$ denotes the net thrust on the ith swimmer.

Here, we offer a high-level summary of the mean net thrust $\bar{C}_{\mathrm{T,pair}}$ of the side-by-side and anti-phase scenarios. Following the formal analysis of previous studies regarding a flapping foil (Floryan *et al.*, 2017; Van Buren *et al.*, 2017; and Alam and Muhammad, 2020) and an undulating foil (Chao *et al.*, 2022), we use the symbolic regression tool PySR (Cranmer, 2023) to automatically produce an interpretable equation that summarizes the $\bar{C}_{\mathrm{T,pair}}$ data in the present study for schooling swimmers, as seen in the following equation:

$$\bar{C}_{\mathrm{T,pair}} = Re^{0.17} St^{2.03} \lambda^{1.23} - 0.26 Re^{0.19} St^{1.00} \lambda^{0.10} - 6.13 Re^{-0.6}. \quad (3)$$

The summarizing capability of Eq. (3) can be demonstrated in Fig. 3(f), with coefficient of determination reaching $R^2 = 0.953$. For the convenience of the readers' comparison, here we also copy the $\bar{C}_{\mathrm{T,pair}}$ equation by Chao *et al.* (2022) for a single swimmer as

$$\bar{C}_{\mathrm{T,single}} = 0.36 Re^{0.208} St^3 \lambda - 6.13 Re^{-0.6}. \quad (4)$$

We can see that compared with the single swimmer thrust $\bar{C}_{\mathrm{T,single}}$ formula produced by Chao *et al.* (2022), the additional mirror-symmetric swimmer casts an interesting effect on the $\bar{C}_{\mathrm{T,pair}}$ of each schooling member. The wavelength is almost linearly correlated with net thrust as $\bar{C}_{\mathrm{T,pair}} \sim \lambda^{1.23}$ when the Strouhal number and the wavelength are relatively small, with the scaling exponent being slightly larger than $\bar{C}_{\mathrm{T,pair}} \sim \lambda^{1.00}$. So the wavelength is slightly more influential to the thrust during schooling compared with the single swimming condition. On the other hand, the primary scaling of thrust coefficient with the Strouhal number is reduced from $\bar{C}_{\mathrm{T,single}} \sim St^3$ for a single foil (Chao *et al.*, 2022) to $\bar{C}_{\mathrm{T,pair}} \sim St^2$ in Eq. (3) with an additional negative term as $-0.26 Re^{0.19} St^{1.00} \lambda^{0.10}$, so the contribution from the Strouhal number to net thrust becomes less significant for the present schooling scenario compared with the single swimmer case. In contrast, the scaling exponent of 2.03 in Eq. (3) is very close to that of two side-by-side pitching foils, which scale as $\bar{C}_{\mathrm{T,pair}} \sim St^2$ (Gungor and Hemmati, 2021). In Eq. (3), the third term $-6.13 Re^{-0.6}$ indicates that, for stationary hydrofoils, i.e., $St = 0$, the unseparated boundary layer causes the domination of fluid drag force (Chao *et al.*, 2022). $\bar{C}_{\mathrm{T,pair}}$ increases slowly with Re due to reduced viscous force. As Re grows, the third term diminishes toward zero.

Despite minor scaling for St, side-by-side schooling can lead to significant net thrust amplification $\bar{C}_{\mathrm{T,pair}}/\bar{C}_{\mathrm{T,single}}$ compared with single swimming condition, as seen in Fig. 4. In general, at a higher wavelength $\lambda > 0.4$ and the Strouhal number $St > 0.7$, the net thrust/acceleration from schooling can be higher than a single wavy foil. Furthermore, at $\lambda > 1.1$ and $0.4 < St < 0.45$, the net thrust for each schooling swimmer can be more than ten times larger than a single swimmer. A lower Reynolds number amplifies the schooling advantage for thrust. This advantageous range of St and λ also corresponds well with the natural *carangiform* fish species with $St \approx 0.4$ (Borazjani and Sotiropoulos, 2008). So a better thrust performance can be another reason to school together in addition to energy conservation (Daghooghi and Borazjani, 2015; Li *et al.*, 2020). This observation might be able to explain why fish school together from the perspective of net thrust; such acceleration can be significant for the predator–prey interaction (Triantafyllou *et al.*, 2016), thus being correlated with the survivorship of swimmers. The maximum amplification factor is obtained at $Re = 1000$ reaching $\bar{C}_{\mathrm{T,pair}}/\bar{C}_{\mathrm{T,single}} = 13$ at $St = 0.3$ and $\lambda = 2$, as illustrated in Fig. 4(a). Maximum amplification factor $\bar{C}_{\mathrm{T,pair}}/\bar{C}_{\mathrm{T,single}}$ generally drops with the Reynolds number, as demonstrated in Fig. 4(f). This result indicates that a higher wavelength $\lambda = 2$ is advantageous for a single swimmer accelerating from low speed/Reynolds number (Du Clos *et al.*, 2019) and even more beneficial for each schooling swimmer. In addition, we should note that schooling can be less advantageous than swimming alone at $\bar{C}_{\mathrm{T,pair}}/\bar{C}_{\mathrm{T,single}} < 1$, located at $0.5 < \lambda < 0.7$ and $St > 0.45$, although in the present parametric space, schooling can yield much better performance in most cases.

B. Dependence of net propulsive efficiency on *St*, *λ*, and *Re*

The present paper defines net propulsive efficiency as $\eta_i = \bar{C}_{\mathrm{T,pair}}/\bar{C}_{\mathrm{P}}$. We note that this formula measures how efficiently the input power is converted to the net thrust, i.e., acceleration (Maertens *et al.*, 2015), as the present study is meant to focus on the problem of acceleration. More discussion and review of the recent development in the efficiency metrics can be found in the appendix from Lin *et al.* (2023a). Since the two swimmers are placed side-by-side in anti-phase, the deforming solid is mirror-symmetric in time and space. Therefore, the resulting flow pattern is symmetrical for most cases in the present study (discussed later in detail). As a result, the thrust for each schooling member can be equivalent to each other $\eta_1 = \eta_2$ in most cases. So in the present study, net propulsive efficiency is represented by averaging the values from each of the two schooling swimmers $\eta = (\eta_1 + \eta_2)/2$.

Net propulsive efficiency η is generally higher in the range of $St > 0.4$ and $0.8 < \lambda < 1.5$, as seen in Fig. 5. The highest efficiency is obtained at $\lambda = 1.1, 1.2$ with $St = 0.50, 0.55$. The optimal Strouhal number $St = 0.5$ matches the observed value for a single linear-accelerating fish, e.g., Crevalle jack (Akanyeti *et al.*, 2017), but slightly higher than that for most steady-swimming fish in nature (Borazjani and Sotiropoulos, 2008). The maximum efficiency and high-efficiency region $\eta > 24\%$ both increase with the Reynolds number. The highest efficiency increases almost linearly with the Reynolds number, which indicates that thrust generation can be less energy-consuming at a higher swimming/flow speed. The high-efficiency band is approximately located on the line $\lambda + 3St = 2.9$, which means that to achieve high efficiency, swimmers cannot choose both high wavelength $\lambda > 1.5$ and high Strouhal number $St > 5.5$ at the same time.

Net propulsive efficiency for mirror-symmetric schooling η_{pair} can be much higher than that of single swimming η_{single}, reaching $\eta_{\mathrm{pair}}/\eta_{\mathrm{single}} = 5$, as seen in Fig. 6. The thick line indicates the locations where $\eta_{\mathrm{pair}}/\eta_{\mathrm{single}} = 1$, i.e., schooling and single swimming yields identical propelling efficiency. It is seen that schooling can be more efficient at $0.25 < St < 0.55$ and $\lambda > 1$. The schooling efficiency can be several times higher than a single swimmer, especially at $St = 0.3$

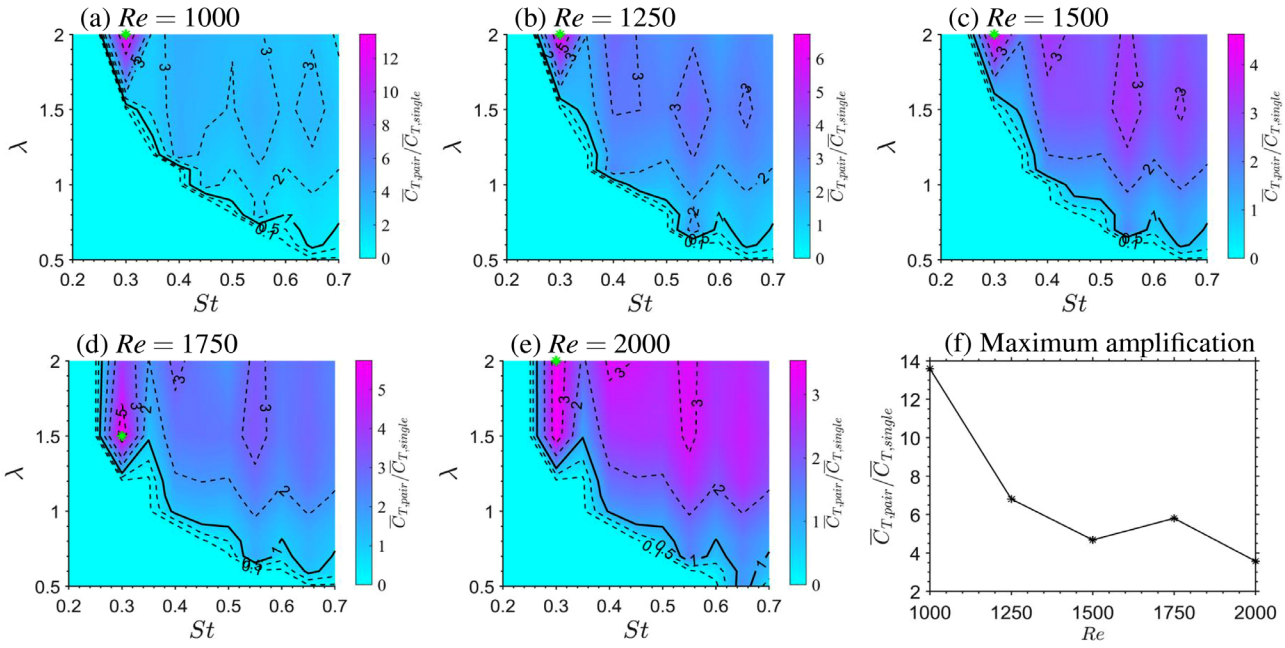

FIG. 4. Heat map for schooling thrust amplification factor $\bar{C}_{T,pair}/\bar{C}_{T,single}$ at the Strouhal number $St = 0.2 - 0.7$, the wavelength $\lambda = 0.5 - 2$, and the Reynolds numbers at (a) $Re = 1000$, (b) $Re = 1250$, (c) $Re = 1500$, (d) $Re = 1750$, (e) $Re = 2000$, and (f) Maximum thrust amplification due to schooling. Here, we only show the results with both $\bar{C}_{T,pair} > 0$ and $\bar{C}_{T,single} > 0$; other non-accelerating cases are drawn as zero. This map demonstrates how schooling contributes to the thrust/acceleration of the swimmers. The thick contour line of $\bar{C}_{T,pair}/\bar{C}_{T,single} = 1$ indicates that thrust from schooling equals that from a single foil. $\bar{C}_{T,pair}/\bar{C}_{T,single} > 1$ means that each schooling member produces higher thrust than a single swimmer, and vice versa for $\bar{C}_{T,pair}/\bar{C}_{T,single} < 1$. The green marker denotes the location for the highest thrust amplification for each Reynolds number. At high St and λ, schooling can produce more thrust. Furthermore, the schooling thrust can be several times higher than a single swimmer, especially at $St = 0.3 - 0.35$ and $\lambda \leq 1.5$. A lower Reynolds number amplifies the schooling advantage for thrust. This advantageous range of St and λ also corresponds well with a single *carangiform* fish at $St \approx 0.4$ (Borazjani and Sotiropoulos, 2008) and other swimming and flying animals at $0.2 < St < 0.4$ (Taylor *et al.*, 2003; Triantafyllou *et al.*, 1991). So a better thrust performance can be another reason to school together in addition to energy conservation (Daghooghi and Borazjani, 2015; Li *et al.*, 2020).

–0.35 and $\lambda \leq 1.5$. A lower Reynolds number amplifies the schooling advantage for efficiency. In short, mirror-symmetric schooling can be more advantageous at low Reynolds numbers and Strouhal numbers, but higher wavelengths.

In addition, for clarification, given steady swimming condition, the Strouhal number of fish swimming ranges from 0.25 to 0.4 (Borazjani and Sotiropoulos, 2008). However, in the present study, we focus on the fish swimming with linear acceleration condition, which can be slightly different. The optimal Strouhal number for efficient force production can reach $St \approx 0.5$ for certain fish species (Akanyeti *et al.*, 2017). For example, Crevalle jack, Indo-Pacific tarpon, and Mangrove snapper achieve optimal propulsive efficiency at $St = 0.51, 0.48, 0.48$, which means that the optimal Strouhal number of 0.5 concluded in the present study actually matches the biological observations for at least some fish species.

C. Flow structures maps

Here, we classify the flow structures of various scenarios based on the overall characteristics, vortex shedding, and flow symmetry. In the parametric space of the present study, we can classify the flow structures into six types: (a) steady wake, (b) quasi-Karman wake, (c) 2S, (d) 2P-diverge, (e) 2P-converge, and (f) symmetry breaking, as demonstrated in Fig. 7. The first five types are mirror-symmetric in time and space, whereas the sixth type demonstrates a chaotic flow structure with symmetry breaking. Here, we explain the main characteristics of each type:

(a) Steady wake: steady streaming in the far field without vortex formation
(b) Quasi-Karman wake: intermediate state between steady streaming and Karman vortex shedding
(c) 2S: a single vortex shed from each wavy foil per cycle, forming a vortex dipole with the main streaming direction pointing downstream
(d) 2P-diverge: one vortex dipole per cycle per foil, forming two reverse vortex streets toward diverging directions
(e) 2P-converge: similar to 2P-diverge, yet the vortex dipoles are converging instead of diverging
(f) Symmetry breaking: symmetrical wake breaks, resulting asymmetric flow pattern

This intensity of vorticity and irregularity both increases with the order listed above. For example, the steady wake (a) contains the lowest overall vorticity intensity with stable flow structures, and vice versa for the symmetry breaking (f) case.

Based on this classification, we generate a set of maps to illustrate the distribution of flow structures in the present parametric space, as shown in Fig. 7; the detailed demonstration for all cases can be found in Appendix A. The markers correspond to the types listed in Fig. 7.

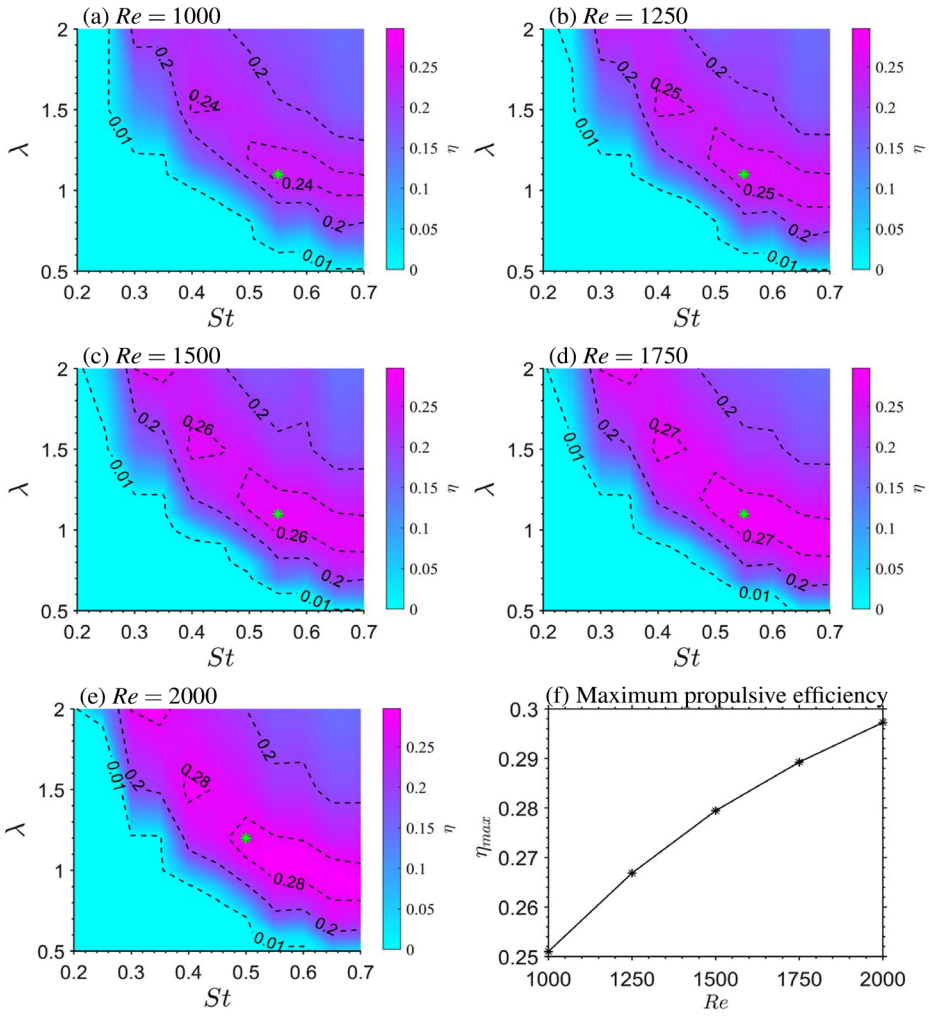

FIG. 5. Heat map for net propulsive efficiency η at the Strouhal number $St = 0.2 - 0.7$, the wavelength $\lambda = 0.5 - 2$, and the Reynolds numbers at (a) $Re = 1000$, (b) $Re = 1250$, (c) $Re = 1500$, (d) $Re = 1750$, and (e) $Re = 2000$. (f) Maximum net propulsive efficiency η_{max} at each Reynolds number. Due to spatial symmetry at any instant, net propulsive efficiency is identical for each swimmer or two swimmers as a group. The highest efficiency is denoted by the green star marker, located at $(St, \lambda) = (0.55, 1.1)$ for $Re = 1000 - 1750$ and $(St, \lambda) = (0.5, 1.2)$ for $Re = 2000$. The optimal Strouhal number $St = 0.5$ matches the observed value for a single linear-accelerating fish, e.g., Crevalle jack (Akanyeti *et al.*, 2017), but slightly higher than that for most steady-swimming fish in nature (Borazjani and Sotiropoulos, 2008). The maximum efficiency and high-efficiency region $\eta > 24\%$ both increase with the Reynolds number. The cases with negative thrust are drawn as zero. The maximum efficiency increases almost linearly with the Reynolds number.

In general, the variation of $Re = 1000$–2000 is not significantly affecting the flow structure distribution, so we mainly discuss the effects of λ and St. The steady wake (a) is only observed at a very low wavelength $\lambda \leq 0.6$ and the Strouhal number $St \leq 0.3$, where the flow is not heavily disturbed. The quasi-Karman wake (b) is observed at slightly higher λ and St, and even higher for the 2S (c) cases. The conversion from quasi-Karman wake (b) to 2S (c) occurs at approximately $4.67St + \lambda = 2.367$. 2P-diverge (d) accounts for the most number of cases in the present study. The transition from 2S (c) to 2P-diverge (d) is observed at approximately $4.5St + \lambda = 2.85$. 2P-converge (e) can be identified at roughly $2.67St + \lambda = 3.067$. The 2P-converge is a boundary condition between the 2P-diverge (d) and the full development of symmetry breaking (f), so only a few cases can be discovered. Furthermore, at $2.67St + \lambda > 3.067$, the flow becomes asymmetric and highly irregular.

The region of high net thrust from Fig. 3 corresponds to the symmetry breaking (f) region in Fig. 8. Zero net thrust cases, i.e., steady-swimming, partly overlap with the boundary between 2S (c) and 2P-diverge (d). So the positive net thrust, i.e., acceleration, mainly corresponds with flow structures of 2P-diverge (d), 2P-converge (e), and symmetry breaking (f). High thrust is found in the symmetry breaking (f) condition, so the irregular flow pattern does not significantly affect the thrust generation. The region of high net propulsive efficiency from Fig. 5 overlaps with the distribution of the 2P-diverge (d) pattern in Fig. 8. Cases with the highest efficiency all demonstrate 2P-diverge (d) pattern. Therefore, the structural vortex dipole shedding contributes to higher efficiency. Conversely, the symmetry breaking (f) region cannot yield high efficiency. While comparing schooling thrust amplification in Fig. 4 and the flow structure map of Fig. 8, it is interesting to note that the most significant schooling amplification factor $\bar{C}_{T,pair}/\bar{C}_{T,single}$ is all located in the 2P-converge (e) region, which corresponds to the s-RKV region of a single swimmer (Chao *et al.*, 2022), featuring a skewed reverse Karman vortex street. This indicates that schooling members can produce more thrust from two converging skewed vortex streets.

D. Investigation of fluid mechanism

The Reynolds number, the wavelength, and the Strouhal number show substantial variations that ultimately result in a distinct difference in the flow structure and corresponding underlying mechanisms. Concurrent with the variation in flow structure, significant changes in

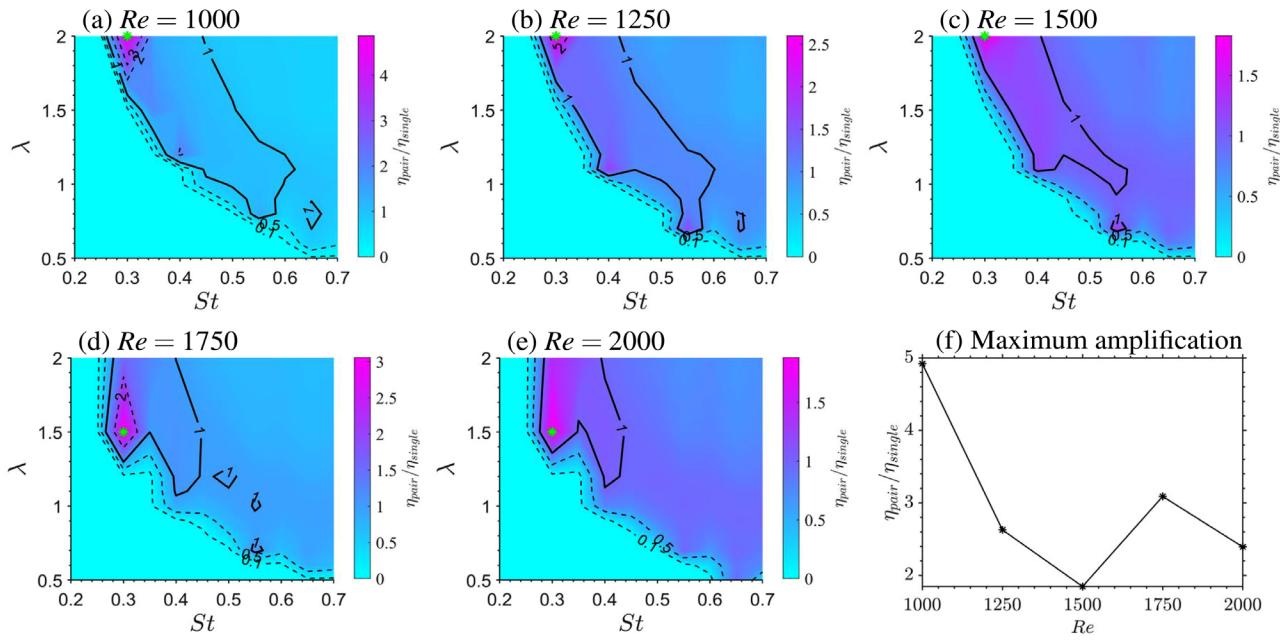

FIG. 6. Heat map for schooling efficiency amplification factor $\eta_{pair}/\eta_{single}$ at the Strouhal number $St = 0.2 - 0.7$, the wavelength $\lambda = 0.5 - 2$, and the Reynolds numbers at (a) $Re = 1000$, (b) $Re = 1250$, (c) $Re = 1500$, (d) $Re = 1750$, (e) $Re = 2000$, and (f) Maximum efficiency amplification at each Re due to schooling. Here, we only show the results with both $C_{T,pair} > 0$ and $C_{T,single} > 0$, and the non-accelerating cases are drawn as zero. This map demonstrates how schooling contributes to the propulsive efficiency of the swimmers. The thick contour line of $\eta_{pair}/\eta_{single} = 1$ indicates equivalent propulsive efficiency from schooling and of a single foil. $\eta_{pair}/\eta_{single} > 1$ means that schooling swimmers produces higher propulsive efficiency than a single swimmer, and vice versa for $\eta_{pair}/\eta_{single} < 1$. The green marker denotes the location for the highest efficiency amplification for each Reynolds number. The schooling efficiency can be several times higher than a single swimmer, especially at $St = 0.3 - 0.35$ and $\lambda \leq 1.5$. A lower Reynolds number amplifies the schooling advantage for efficiency.

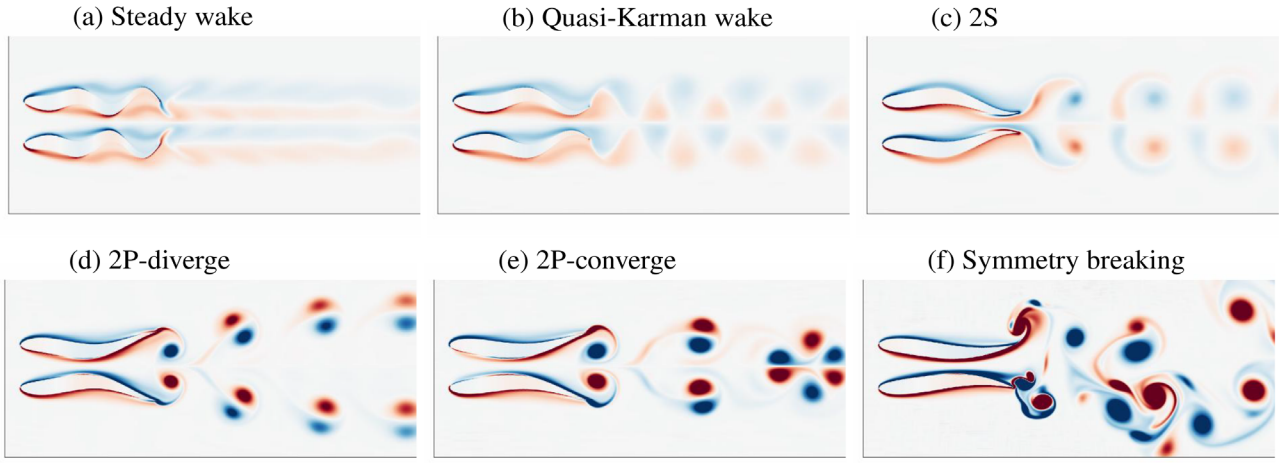

FIG. 7. Representative examples for six flow structures identified as: (a) steady wake: steady streaming in the far-field wake, (b) quasi-Karman wake: periodically disturbed wake but no distinct vortex, (c) 2S: one vortex from each foil, (d) 2 P-diverge: a pair of vortices diverging in the wake, (e) 2P-converge: a pair of vortices converging in the wake, (f) symmetry breaking: an unstable flow that is asymmetric Here, the red color denotes positive vorticity (counterclockwise) with the blue color representing the negative vorticity (clockwise).

performance metrics, i.e., thrust and efficiency, are observed. In this section, to delve deeper into the mechanisms, three typical cases are selected for a detailed analysis and comparative study. The cases are analyzed using fluid vorticity, net force, pressure distribution, and fluid velocity vectors.

The selected cases for our investigation are presented in Table III. Each case represents a consistent increment in input values: the Reynolds number increases by 500, the Strouhal number by 0.1, and the wavelength by 0.3. These cases are chosen to represent different flow structures, namely, 2S in the first case, 2P-diverge in the second

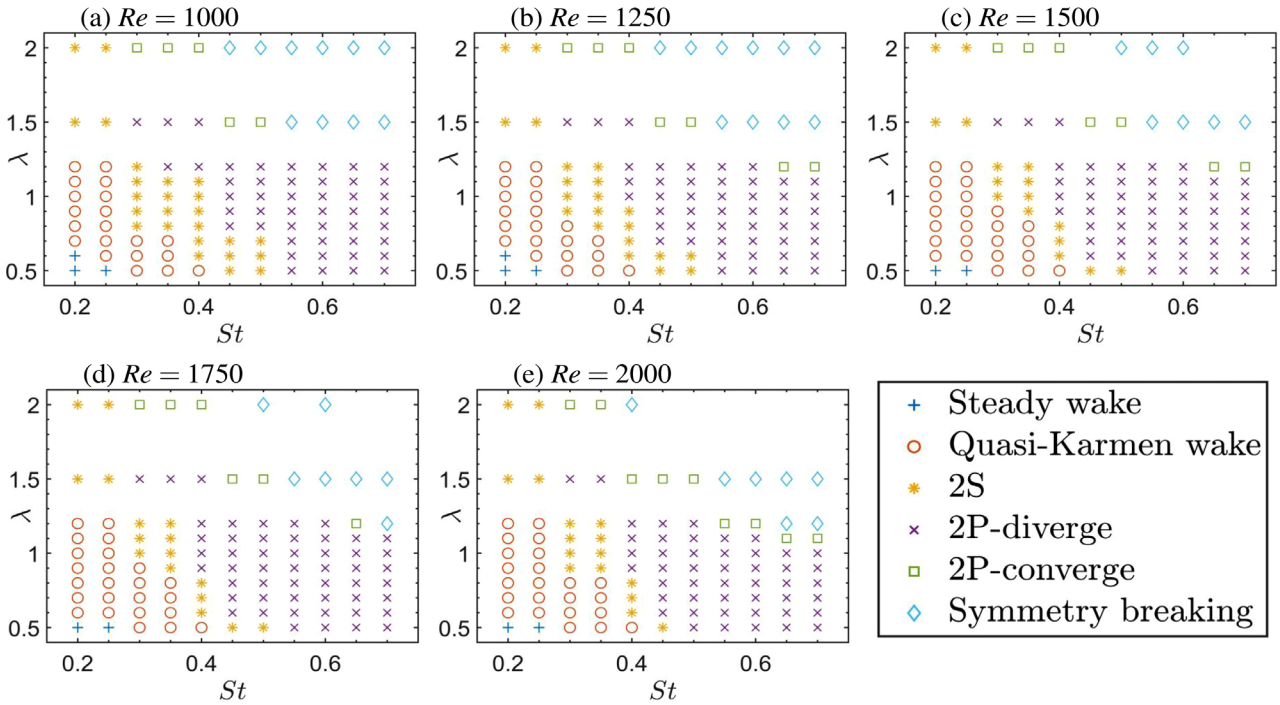

FIG. 8. Flow structure classification at the Strouhal number $St = 0.2$–0.7, the wavelength $\lambda = 0.5$–2, and the Reynolds numbers at (a) $Re = 1000$, (b) $Re = 1250$, (c) $Re = 1500$, (d) $Re = 1750$, and (e) $Re = 2000$. The alphabetic marker types correspond to the classification shown in Fig. 7.

TABLE III. Representative cases for in-depth study and comparison.

No.	Re	St	λ	Flow structure	$\bar{C}_{T,pair}$	η_{pair}	Vorticity and force	Pressure and velocity
First	1000	0.4	0.9	2S [Fig. 7(c)]	−0.059	N/A	Fig. 9	Fig. 10
Second	1500	0.5	1.2	2P-diverge [Fig. 7(d)]	0.403	27.5%	Fig. 11	Fig. 12
Third	2000	0.6	1.5	Sym breaking [Fig. 7(f)]	1.527	21.4%	Fig. 13	Fig. 14

case, and symmetry breaking in the third case. To facilitate comparison, we maintain identical color scales for vorticity, pressure, and velocity vectors across these cases.

In the first case at $Re = 1000$, $St = 0.4$, and $\lambda = 0.9$, each hydrofoil sheds two vortices per undulation cycle. The generated thrust force profiles are nearly identical between the hydrofoils, with peak thrust corresponding to the shedding of stronger vortices [Figs. 9(i)–9(j)]. The primary pressure fluctuation occurs between the swimmers (Fig. 10), with high thrust related to high downstream fluid velocity and rapid dissipation of negative pressure downstream. A two-row vortex array accounts for velocity vector fluctuations in the wake.

The similarity in the thrust force profiles between the two swimmers [Figs. 9(i)–9(j)] is noteworthy, with two peaks at instants c and g associated with maximum instantaneous thrust. Interestingly, the shedding of the stronger vortex corresponds to the higher thrust peak at instant c, while the formation of a smaller, short-lived vortex results in a smaller thrust peak at instant g. On the contrary, the thrust trough at instant h corresponds to the complete shedding of the minor vortex, which lacks the necessary strength to generate sufficient thrust. Significant pressure fluctuations primarily occur in the gap between the two swimmers, as illustrated in Fig. 10. The maximum positive pressure, which aligns with low thrust, is attained at the instant a in the gap, resulting in a high lift force that separates the swimmers. In contrast, at instants e, the pressure in the gap hits a negative maximum, where the thrust is close to the local minimum, and the lift turns positive, drawing the swimmers together.

Furthermore, high thrust at instants b is achieved when strong positive pressure is exerted at the posterior part of the swimmers, propelling them forward. At instant c, the swimmers are "sucked" forward due to strong negative pressure at their front. In the downstream area, the vortex shedding creates negative pressure [Fig. 10(g)], which dissipates rapidly within one cycle. By analyzing the velocity field, we discovered that high thrust aligns with high fluid velocity toward the downstream direction, "propelling" the swimmers forward. The two-row vortex array in the wake introduces velocity vector fluctuations that follow a similar pattern.

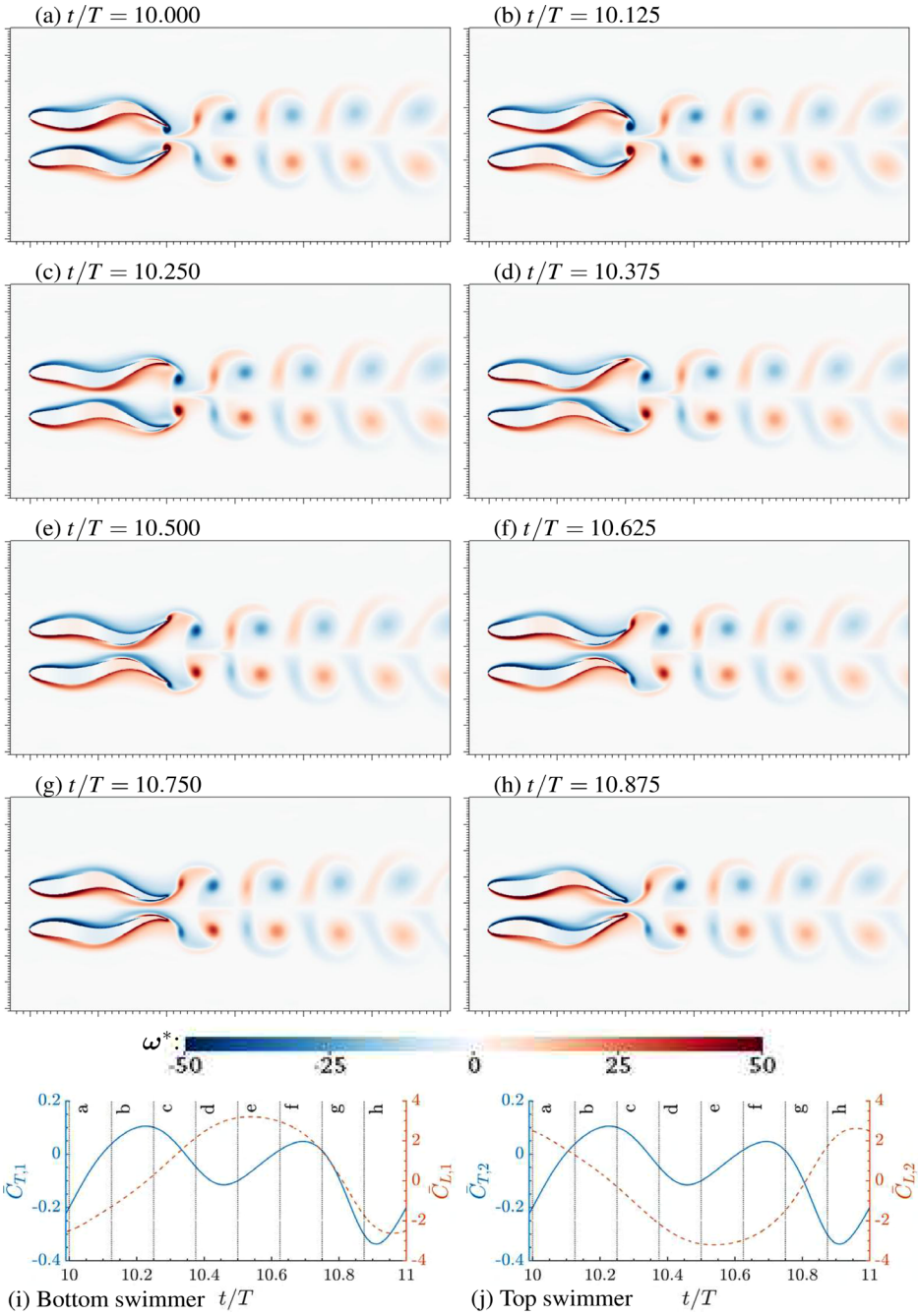

FIG. 9. Vorticity contours and hydrofoil deformation with $Re = 1000$, $St = 0.4$, and $\lambda = 0.9$, at instants of a typical period (a-h) $t/T = 10.000 - 10.875$. Time histories of thrust and lift coefficient for the (i) bottom and (j) top swimmers.

In the second case, with $Re = 1500$, $St = 0.5$, and $\lambda = 1.2$, we identify a distinctive "2P-diverge" flow pattern in the wake of the two swimmers, wherein the outer vortex exhibits greater persistence and influences the vortex direction alignment. Instances of simultaneous high pressures at the ends of the swimmers produce high net thrust.

Observation of the vorticity distribution (Fig. 11) reveals that two distinct rows of vortex dipoles are propelled from the swimmers' posterior part, forming the unique 2P-diverge flow structure pattern, contrasting markedly with the "2S" pattern of the first case. The vortex shedding mechanism is similar to the first case, with each undulation cycle of the hydrofoils generating two vortices. However, the outer vortex persists rather than dissipating, resulting in vortex dipoles propelled away from the mirror-symmetric axis between the swimmers. The outer vortex's rapid dissipation compared to the inner one can be ascertained from the vorticity and pressure distribution (Figs. 11 and 12). As the dissipation progresses, the vortex dipoles' moving direction

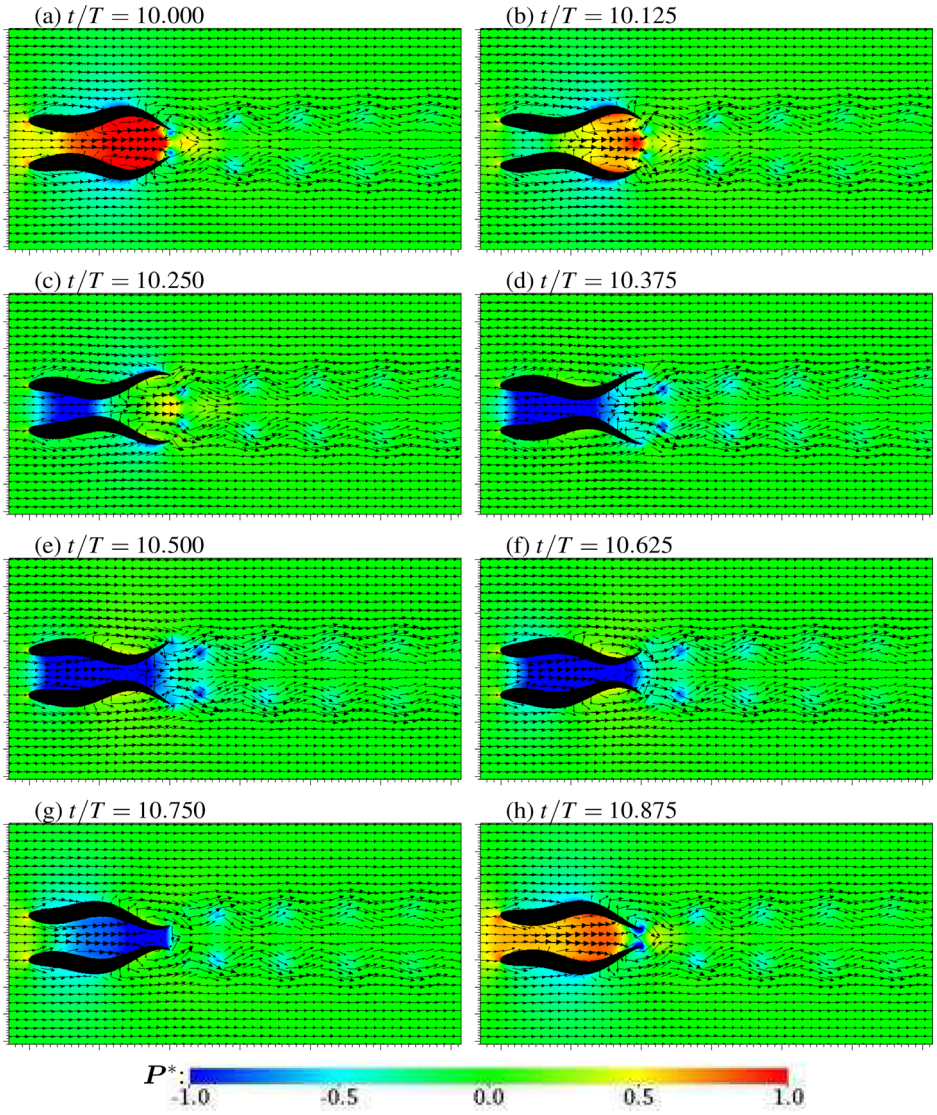

FIG. 10. Pressure contours, velocity vectors, and hydrofoil deformation with $Re = 1000$, $St = 0.4$, $\lambda = 0.9$, at instants of a typical period (a)–(h) $t/T = 10.00 - 10.875$. Time histories of thrust and lift coefficient for the (i) bottom and (j) top swimmers.

gradually aligns with the free-stream velocity. Mirroring the first case, the time history of the thrust force features two peaks and one trough. The major and minor peaks are located at instants d and h, respectively. It is intriguing that these instants of high net thrust coincide with high positive and negative pressure at the swimmers' posterior and anterior parts, respectively (Fig. 12). This observation suggests that the swimmer is simultaneously "pushed" and "pulled" by the positive and negative pressure at different locations, contributing to high instantaneous thrust. The larger peak at instant d occurs when positive pressure is on the outside, and negative pressure is in the gap. The thrust at instant h is weaker due to the formation of the vortex pair near the tails, which slightly reduces the pressure in the gap.

In the third case, at $Re = 2000$, $St = 0.6$, and $\lambda = 1.5$, despite irregular wake flow and symmetry breaking, the fluid–structure interaction mechanism aligns largely with the second case exhibiting the 2P-diverge pattern. The near-tail flow field maintains substantial regularity and symmetry.

In the third case, as depicted in Figs. 13 and 14, the flow structure exhibits irregularity with symmetry breaking, although the vortices near the tails remain largely regular and symmetric. Like to the second case, each hydrofoil generates a pair of vortices in a complete cycle. The vortex dipoles shed from each foil rapidly converge while interacting with previously generated vortices, leading to irregularity in the flow field. This pattern differs from the second case, where the vortex sheddings symmetrically diverge rather than quickly impinge on each other. Despite the irregular wake flow, the net thrust and lift force time history between the two swimmers remain strikingly identical, as seen in Figs. 13(i) and 13(j). Furthermore, the correlation between pressure distribution and force variation strongly resembles to the second case with the 2P-diverge pattern. High thrust is observed when the

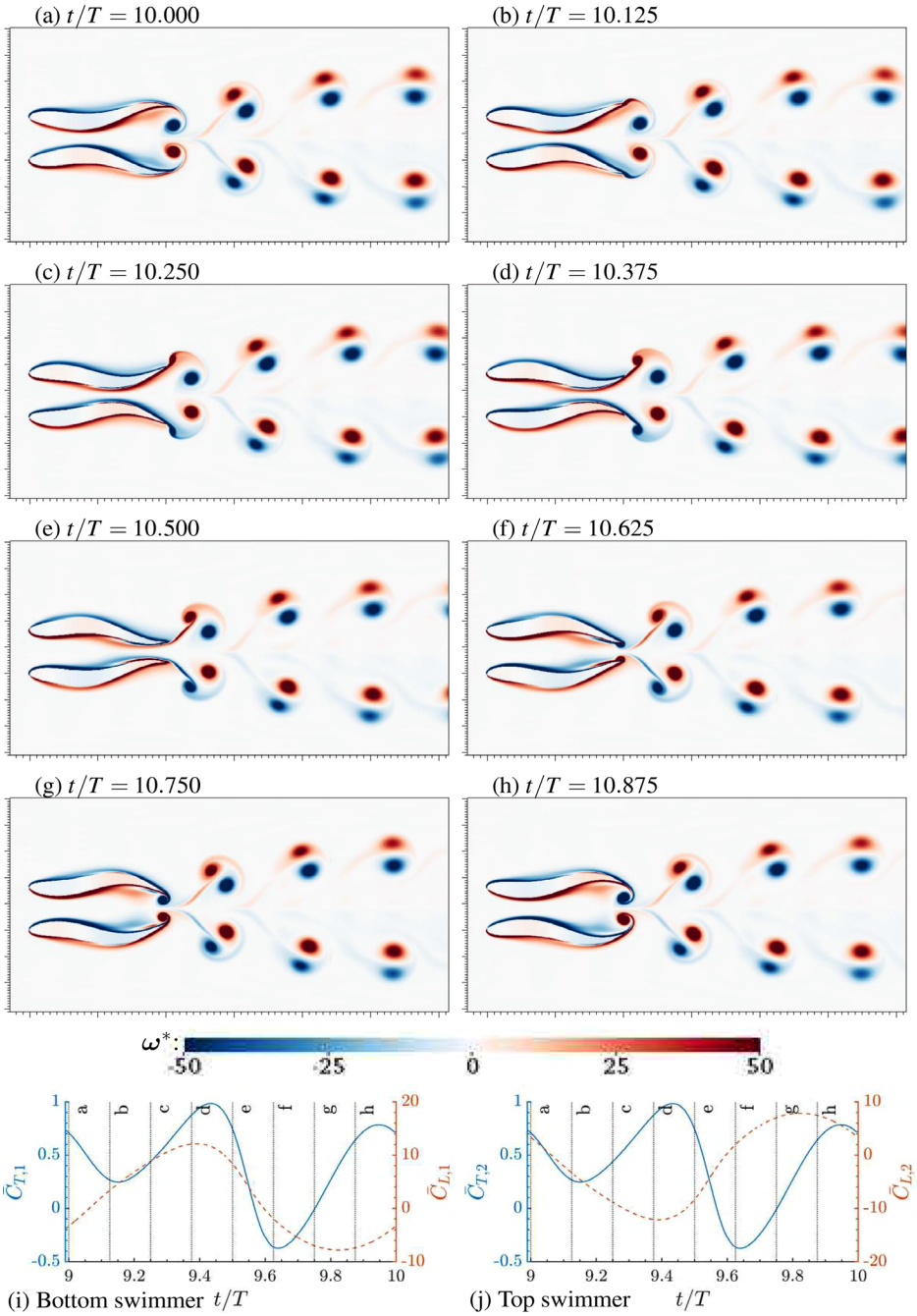

FIG. 11. Vorticity contours and hydrofoil deformation with $Re = 1500$, $St = 0.5$, and $\lambda = 1.2$, at instants of a typical period (a)–(h) $t/T = 10.00 - 10.875$. Time histories of thrust and lift coefficient for the (i) bottom and (j) top swimmers.

swimmers are pushed and pulled by the positive and negative pressure at the posterior and anterior parts of the hydrofoil body. However, the vortex pair in the gap slightly mitigates the thrust at instant g, as seen in Fig. 14(g). Regarding the wake region, here, the pressure disturbance is significantly more pronounced compared with the previous cases, due to the strong negative pressure created by the recirculation and interaction of the vortices.

IV. CONCLUSIONS

The effects of fish body wavelength on its linear acceleration during side-by-side schooling conditions have not been studied in detail previously. In the present paper, we conducted a systematic numerical study, involving 550 cases of two linearly accelerating side-by-side wavy NACA0012 hydrofoils swimming in anti-phase. We examined the net thrust distribution, net propulsive efficiency, and flow

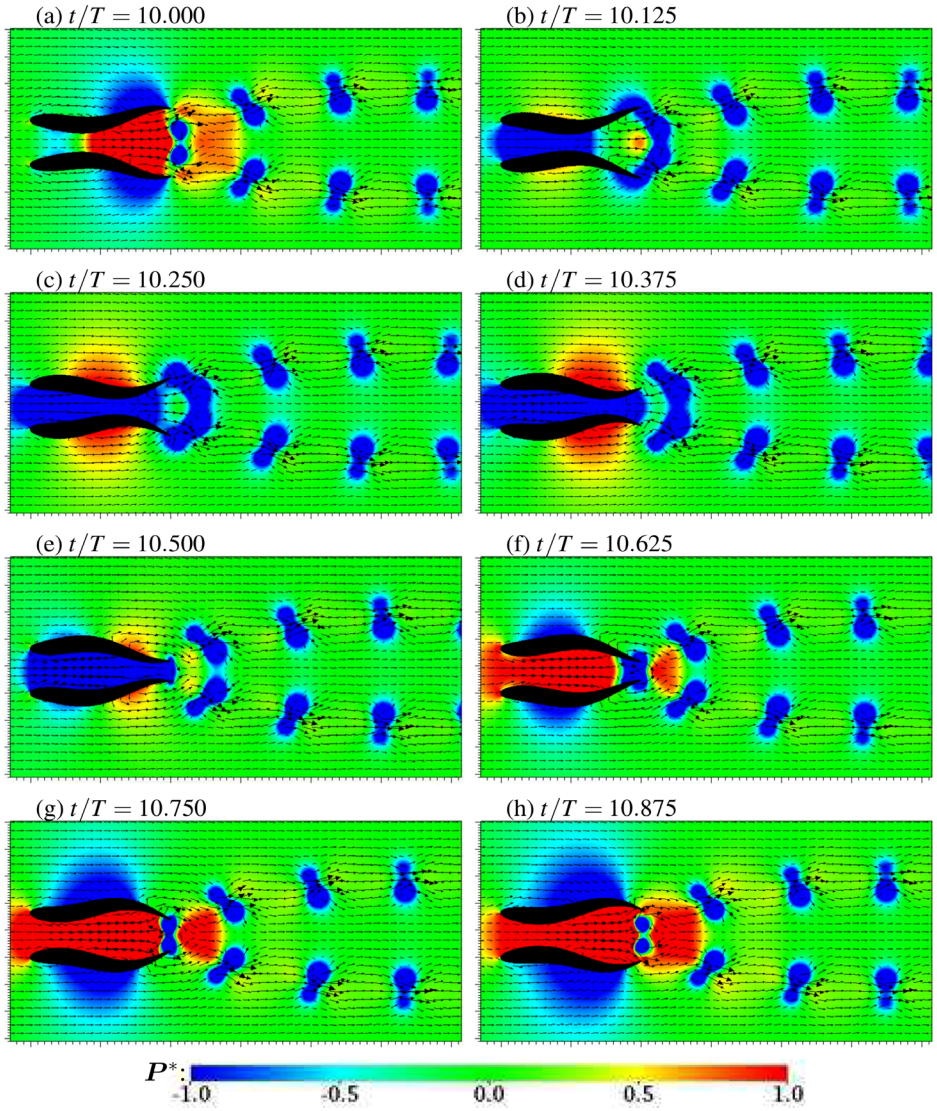

FIG. 12. Pressure contours, velocity vectors, and hydrofoil deformation with $Re = 1500$, $St = 0.5$, and $\lambda = 1.2$, at instants of a typical period (a)–(h) $t/T = 10.00 - 10.875$. Time histories of thrust and lift coefficient for the (i) bottom and (j) top swimmers.

structures by drawing heat maps and proposing empirical formulas. The simulation is conducted on a customized version of the ConstraintIB (Bhalla *et al.*, 2013; Griffith and Patankar, 2020) module from the IBAMR (Griffith, 2013) open-source library. The parametric space is tested for the Strouhal number $St = 0.2$–0.7, the wavelength $\lambda = 0.5$–2, and the Reynolds number $Re = 1000$–2000. The lateral gap distance and maximum tail amplitude are fixed at $G = 0.33$ and $A_{max} = 0.1$, respectively. These ranges are chosen based on BCF swimmers in nature (Gazzola *et al.*, 2014; Santo *et al.*, 2021).

Here, we summarize the discoveries as follows:

(1) We propose an equation as a high-level summary of the mean net thrust on each undulating swimmer: $\bar{C}_{T,pair} = Re^{0.17}St^{2.03}\lambda^{1.23} - 0.26Re^{0.19}St^{1.00}\lambda^{0.10} - 6.13Re^{-0.6}$.
(2) Mean net thrust increases with the wavelength λ and the Strouhal number St, yet only slightly with the Reynolds number Re in the present laminar regime. When λ and St are relatively small, the thrust increases almost linearly with the wavelength $\bar{C}_{T,pair} \sim \lambda^{1.23}$ while scaling with the Strouhal number as $\bar{C}_{T,pair} \sim St^2$, where the scaling-exponent being two-thirds of that for a single swimmer $\bar{C}_{T,pair} \sim St^3$ (Chao *et al.*, 2022).
(3) Side-by-side anti-phase schooling can enhance the thrust by more than ten times, as compared with a single swimmer at $\lambda \geq 1.5$ and $St = 0.3$.
(4) High net propulsive efficiency η is achieved at $St > 0.4$ and $0.8 < \lambda < 1.5$, with the highest obtained at about $St = 0.5$ and $\lambda = 1.1$, which are consistent with the biological observations.
(5) We classify the flow structures into six distinct types based on their flow characteristics: (a) steady wake, (b) quasi-Karman wake, (c) 2S, (d) 2P-diverge, (e) 2P-converge, and (f) symmetry breaking.

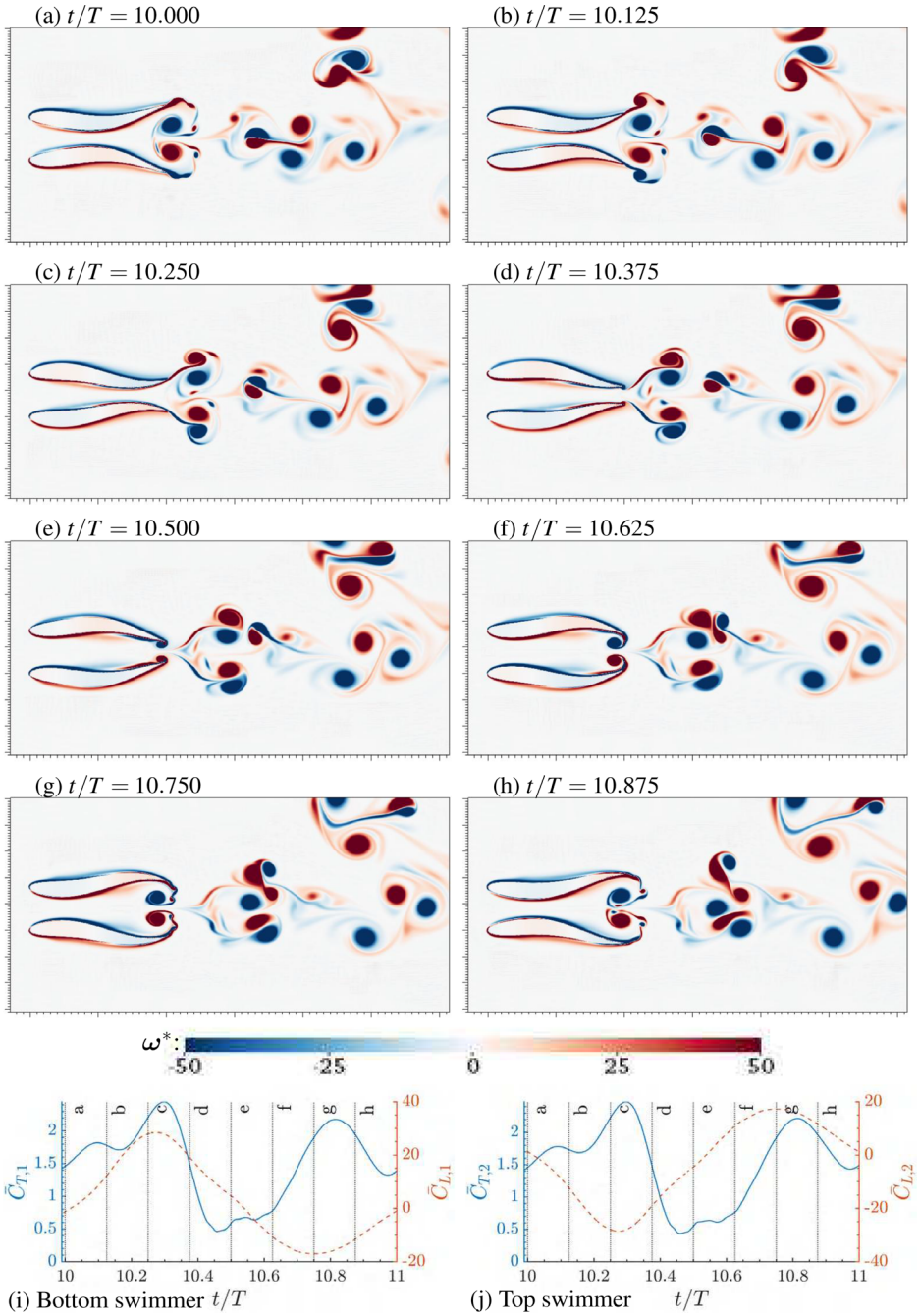

FIG. 13. Vorticity contours and hydrofoil deformation with $Re = 2000$, $St = 0.6$, and $\lambda = 1.5$, at instants of a typical period (a-h) $t/T = 10.00 - 10.875$. Time histories of thrust and lift coefficient for the (i) bottom and (j) top swimmers.

(6) The wavelength λ and the Strouhal number St are more influential than the Reynolds number Re in determining the flow structures in the tested parametric space. The highest net thrust is accompanied with symmetry breaking, whereas the high-efficiency regime corresponds to a 2P-diverge type wake.
(7) Instantaneous high thrust occurs when differential pressure at the rear and front of the hydrofoil body simultaneously "pushes" and "pulls" the swimmers, respectively, while the presence of a vortex pair in the intermediary space diminishes thrust when the tails move outward.

Based on these results, we can make a few interesting comments that help understand the hydrodynamically relevant behavior of biological swimmers in nature or for designing a schooling strategy for biomimetic robotic underwater vehicles. Side-by-side schooling can produce much higher thrust and, therefore, higher acceleration than

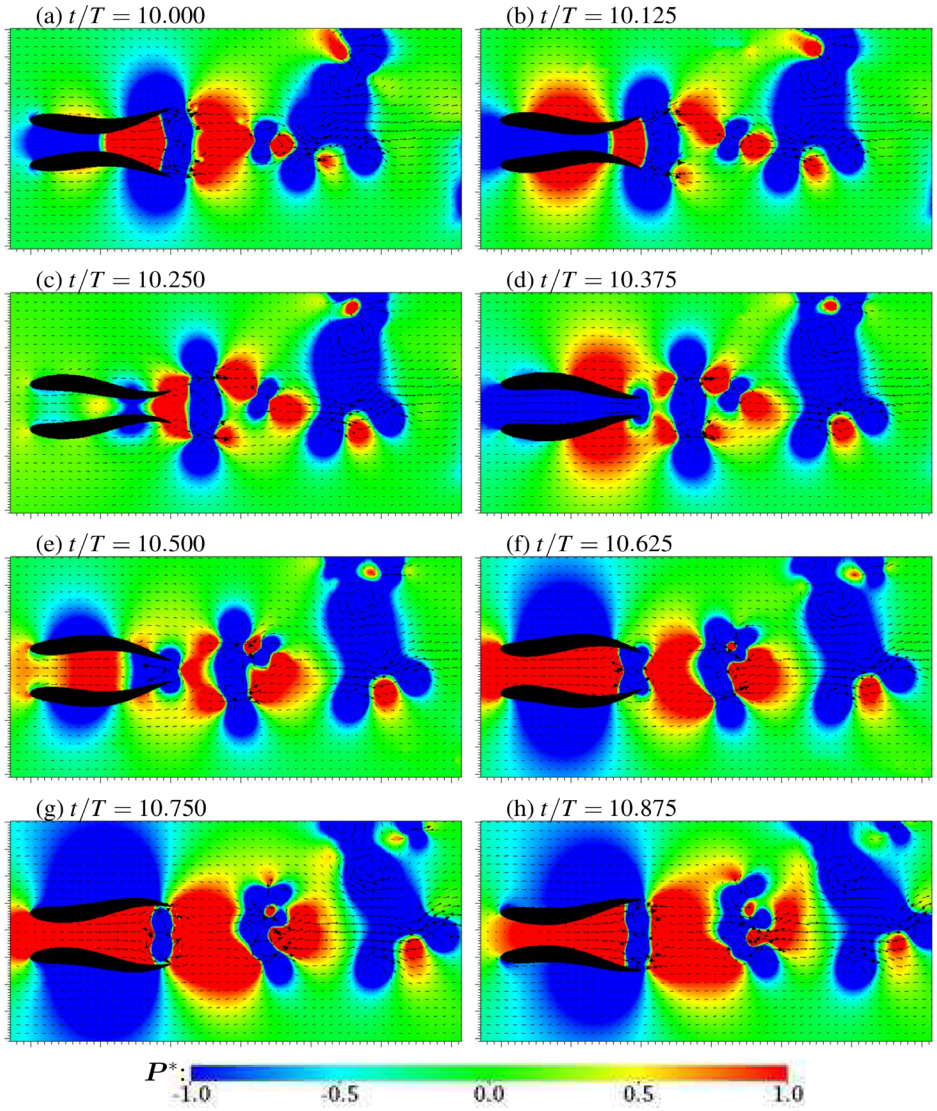

FIG. 14. Pressure contours, velocity vectors, and hydrofoil deformation with $Re = 2000$, $St = 0.6$, and $\lambda = 1.5$, at instants of a typical period (a)–(h) $t/T = 10.00 - 10.875$. Time histories of thrust and lift coefficient for the (i) bottom and (j) top swimmers.

a single BCF swimmer. This schooling advantage is most prominent at low Reynolds numbers, implying that the fish's swimming agility improves in school. Hence, schooling may be preferred due to better survivorship associated with faster acceleration. Also, in the context of schooling conditions considered here, the wavelength and the Strouhal number for best efficiency are $\lambda \approx 1.2$ and $St \approx 0.5$, respectively, which match the observed values for a single swimmer (Borazjani and Sotiropoulos, 2008). In future, Floquet analysis can be further applied to shed light on the symmetry breaking during acceleration.

V. LIMITATIONS AND FUTURE WORKS

The present study involves only 2D simulations, whereas high-fidelity 3D models can be useful to real 3D flow patterns for a few cases, e.g., maximum thrust or efficiency. The present study applies a tethered configuration to approximate various instants of linear acceleration, which is not the most accurate and intuitive method. We will conduct more self-propelling simulations in the future. Also, the conclusions regarding Reynolds number are limited to the present laminar parametric space involving $Re = 1000$–2000. The effects of Re in transition and turbulent regimes remain to be explored in the future. Additionally, further analysis of the underlying mechanism should require examination of added mass and added damping, etc.

ACKNOWLEDGMENTS

This work was funded by China Postdoctoral Science Foundation (Grant No. 2021M691865) and by Science and Technology Major Project of Fujian Province in China (Grant No. 2021NZ033016). We appreciate the U.S. National Science Foundation Award No. OAC 1931368 (A.P.S.B) for supporting the IBAMR library. This work was also financially supported by the National Natural Science Foundation of China (Grant Nos. 12074323 and 42106181), the Natural Science

Foundation of Fujian Province of China (Grant No. 2022J02003), the China National Postdoctoral Program for Innovative Talents (Grant No. BX2021168), and the Outstanding Postdoctoral Scholarship, State Key Laboratory of Marine Environmental Science at Xiamen University. For the purpose of open access, the authors have applied a Creative Commons Attribution (CC BY NC ND) licence to any Author Accepted Manuscript version arising from this submission.

AUTHOR DECLARATIONS

Conflict of Interest

The authors have no conflicts to disclose.

Author Contributions

Zhonglu Lin: Conceptualization (equal); Data curation (equal); Formal analysis (equal); Funding acquisition (equal); Investigation (equal); Methodology (equal); Resources (equal); Software (equal); Validation (equal); Visualization (equal); Writing – original draft (equal); Writing – review & editing (equal). **Dongfang Liang:** Resources (lead); Writing – review & editing (equal). **Amneet Pal Singh Bhalla:** Software (equal); Validation (equal); Writing – review & editing (equal). **Ahmed A. Sheikh Al-Shabab:** Writing – review & editing (equal). **Martin Skote:** Writing – review & editing (equal). **Wei Zheng:** Visualization (equal). **Yu Zhang:** Conceptualization (equal); Funding acquisition (equal); Project administration (equal); Resources (equal); Supervision (equal).

DATA AVAILABILITY

The data that support the findings of this study are available from the corresponding author upon reasonable request.

APPENDIX A: FLOW STRUCTURE MAPS IN DETAIL

This section supplements the detailed flow structure maps in the tested parametric space of our present study. Vorticity contours are drawn to illustrate the flow structures at the Reynolds numbers of $Re = 1000 - 2000$, as seen in Figs. 15–19. These flow structures can be classified into six types, as exemplified by Fig. 7, and the type distribution is illustrated by Fig. 8, as discussed in Sec. III C.

APPENDIX B: DERIVATION OF THRUST AMPLIFICATION FACTOR AND METRICS FOR THRUST AND PROPULSIVE EFFICIENCY

This section expounds on the derivation of the thrust amplification factor and elucidates our choice of metric for propulsive efficiency. The metric for net Froude or propulsive efficiency employed herein is congruent with that used by Akanyeti *et al.* (2017), denoting the efficacy with which the thrust force is generated.

The justification for our computation of the thrust amplification factor lies in the following: given a situation where the net average thrust coefficient for a single foil, $\bar{C}_{\mathrm{T,single}}$, converges to zero — that is, in a steady swimming scenario — the denominator of the thrust amplification factor, $\bar{C}_{\mathrm{T,pair}}/\bar{C}_{\mathrm{T,single}}$, would correspondingly converge to zero. This occurrence results in an exorbitantly large value for the amplification factor. However, our data-processing procedures duly account for this. In the course of our post-processing computation of the thrust amplification factor $\bar{C}_{\mathrm{T,pair}}/\bar{C}_{\mathrm{T,single}}$ and efficiency amplification factor $\eta_{\mathrm{pair}}/\eta_{\mathrm{single}}$, we calculate the amplification factor only if $\bar{C}_{\mathrm{T,pair}} > 0.01$ and $\bar{C}_{\mathrm{T,single}} > 0.01$ — both of which are larger than a pre-established threshold.

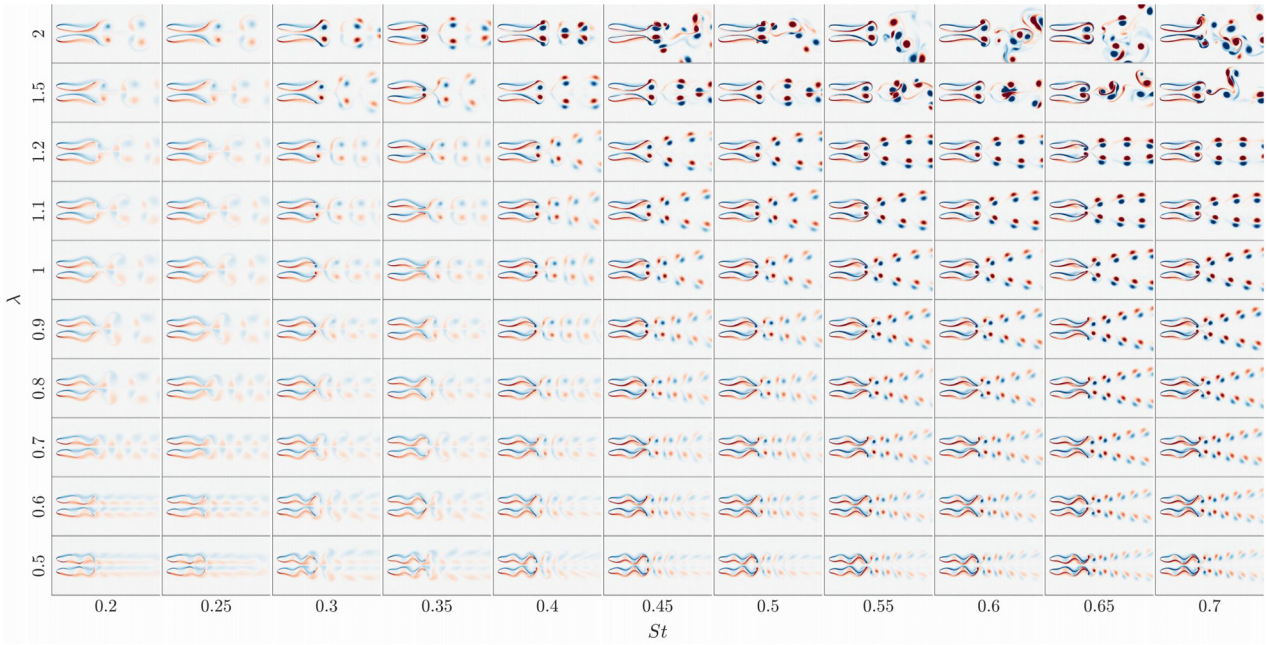

FIG. 15. Flow structure visualized by vorticity contours at $Re = 1000$ with $St = 0.2$–0.7 and $\lambda = 0.5$–2.

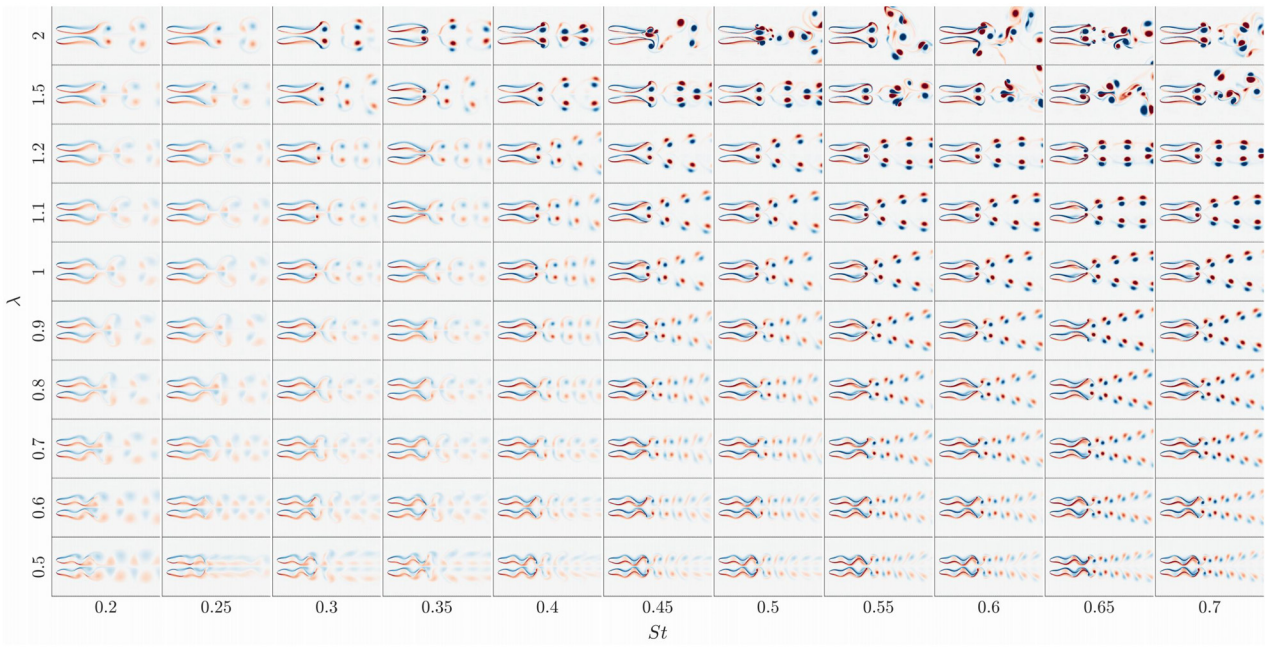

FIG. 16. Flow structure visualized by vorticity contours at $Re = 1250$ with $St = 0.2$–0.7 and $\lambda = 0.5$–2.

If these conditions are not met, the amplification factor is set as zero in the heat maps. The absence of this restriction would have the amplification factor reaching an excessive scale of 10^3 owing to its proximity to zero and numerical discrepancies. The choice of 0.01 ensures a satisfactory distance from zero while considering the potential range of numerical variances.

Delving further into specifics, we discerned that $\bar{C}_{\mathrm{T,pair}} = 0.2289$ while $\bar{C}_{\mathrm{T,single}} = 0.0165$. We thus regard the single swimmer *net* thrust $\bar{C}_{\mathrm{T,single}} = 0.0165$ as sufficiently larger than the steady swimming condition $\bar{C}_{\mathrm{T,single}} \approx 0$, especially in comparison with other results, where the net thrust can approach zero as $\bar{C}_{\mathrm{T,single}} = 2.24 \times 10^{-5} \approx 0$.

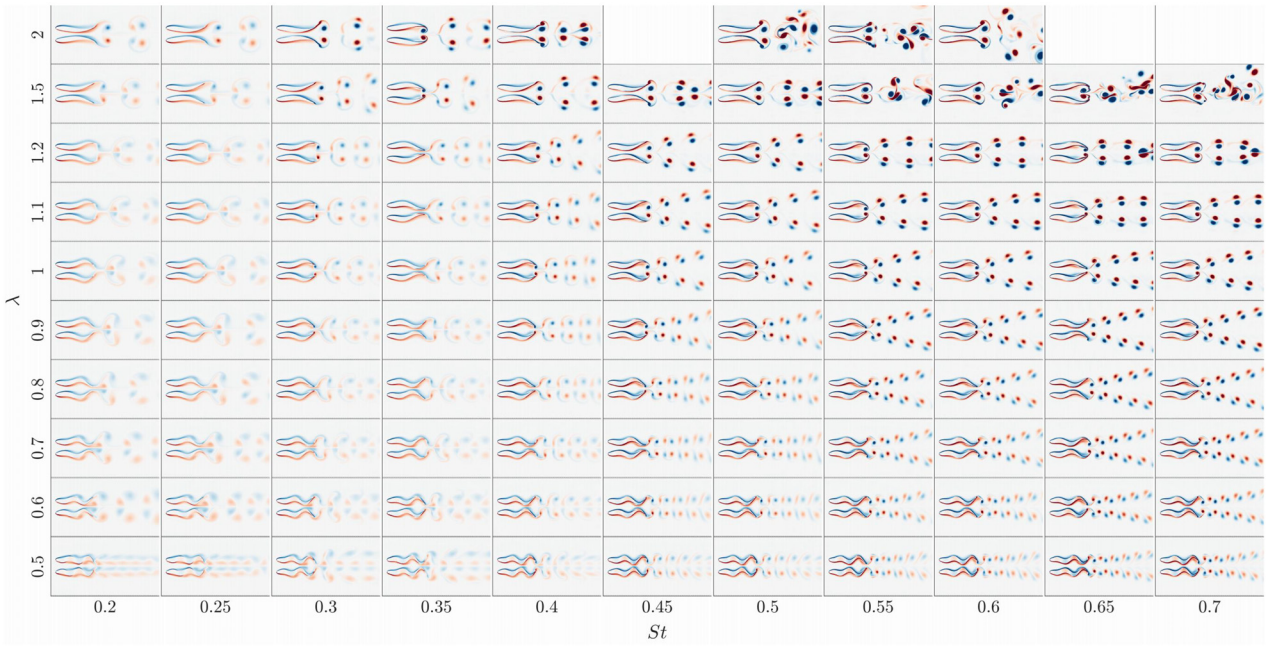

FIG. 17. Flow structure visualized by vorticity contours at $Re = 1500$ with $St = 0.2$–0.7 and $\lambda = 0.5$–2.

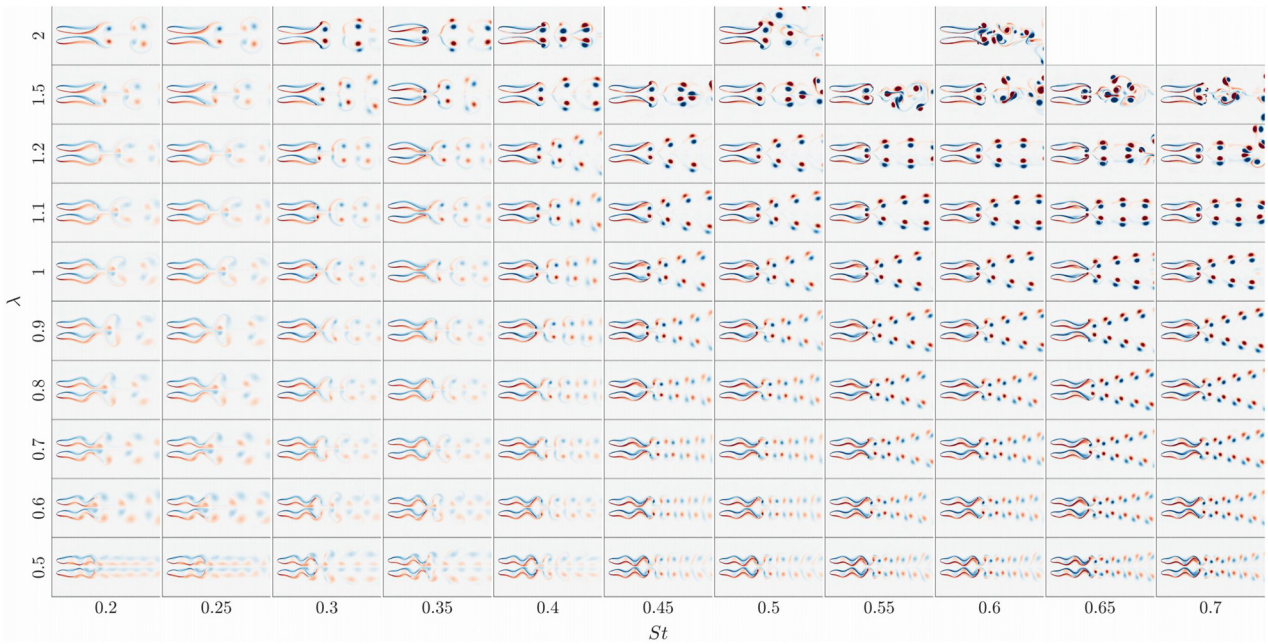

FIG. 18. Flow structure visualized by vorticity contours at $Re = 1750$ with $St = 0.2$–0.7 and $\lambda = 0.5$–2.

This section also examines the definitions of thrust and efficiency. Our study principally addresses the imbalanced situation of linear acceleration, deviating from the steady swimming conditions examined in prior works (Pan and Dong, 2020). Consequently, our chosen metrics are the *net* thrust coefficient and the *net* Froude or propulsive efficiency — that is, the efficiency calculated from net thrust. In the context of this work, the *net* thrust coefficient, $\bar{C}_{\mathrm{T,pair}}$, signifies the net force propelling the swimmer, while the *net* Froude efficiency indicates the proficiency with which the force or acceleration is generated. For an in-depth exploration, we kindly direct the

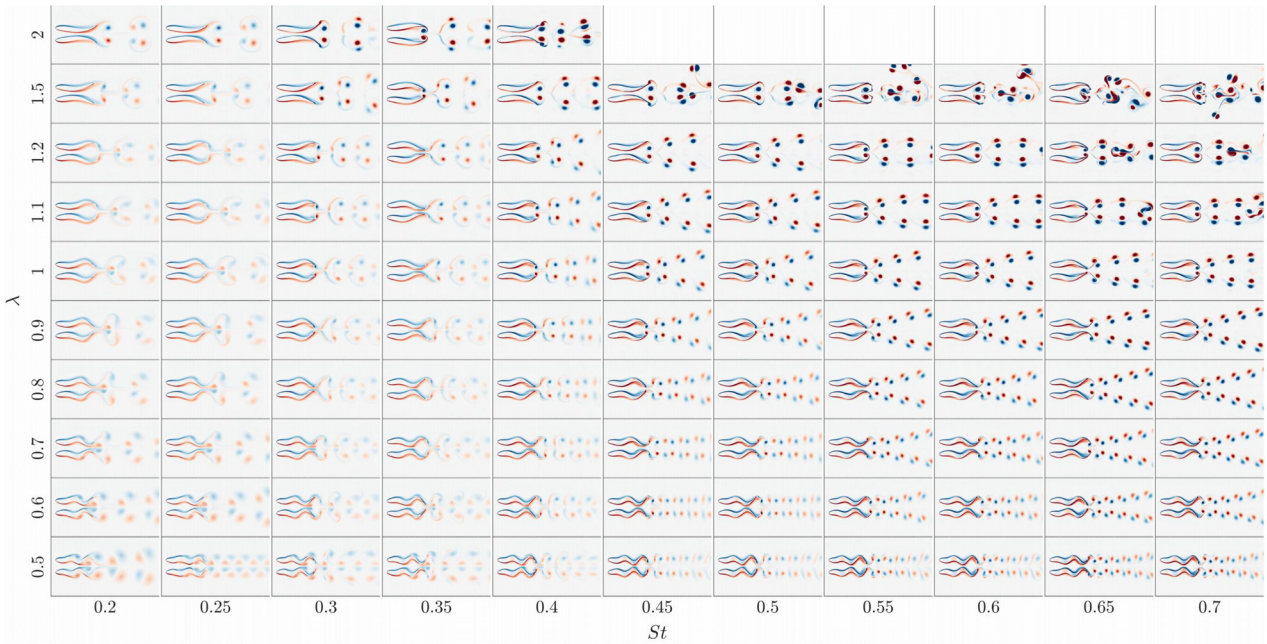

FIG. 19. Flow structure visualized by vorticity contours at $Re = 2000$ with $St = 0.2$–0.7 and $\lambda = 0.5$–2.

reader to our previous publication, which focuses on acceleration Lin *et al.* (2023a), where we have extensively justified our chosen metrics.

The concept of efficiency is identical between the present paper and that by Dong and Lu (2007). The metric is fundamentally the Froude efficiency derived from net thrust as

$$\eta = \frac{\text{Thrust}_{\text{ave}} \times \text{U}}{\text{Power}_{\text{ave}}} = \frac{\overline{C_T}}{\overline{C_P}}. \tag{B1}$$

In their paper "Efficiency of Fish Propulsion," Maertens *et al.* (2015) reviewed numerous extant metrics of "fish swimming efficiency." The "propulsive efficiency" adopted in this paper equates to the "net propulsive efficiency" referenced in Maertens *et al.* (2015), defined in their work as $\eta = \overline{C_T}/\overline{C_P}$. The optimal "net propulsive efficiency" equates to the minimum energy consumption required to attain a given acceleration. This is distinct from the optimal steady swimming efficiency, which sustains a specific velocity with zero acceleration. Maertens *et al.* (2015) proposed a novel metric, quasi-propulsive efficiency, as $\eta = (\overline{C_T} + C_D)/\overline{C_P}$, which incorporates a separately measured drag term. However, we posit that this new metric is better suited for gauging overall swimming performance rather than acceleration performance Maertens *et al.* (2015). For more detailed discussions, please refer to the appendix in our previous publication (Lin *et al.*, 2023a).

Maertens *et al.* (2017) employed quasi-propulsive efficiency, where the "thrust" used for calculation is determined by "towing a rigid body in a static flow with a prescribed velocity." This methodology circumvents the issue of zero net thrust force and consequent zero efficiency during steady swimming – the central focus of the Maertens *et al.* (2017) paper. Contrarily, the current manuscript prioritizes acceleration over steady swimming conditions, wherein the net force is non-zero. Hence, we compute the propulsive efficiency using net thrust instead of the method used by Maertens *et al.* (2017).

Pan and Dong (2020) likewise focused on steady swimming. They used pure thrust – that is, without considering the drag – rather than net thrust, to calculate a modified form of Froude efficiency as $\eta = FU/(FU + P_{\text{wake}})$, where P_{wake} denotes the power in the wake.

In summary, the calculation of thrust amplification factor and the chosen efficiency metric of net Froude or propulsive efficiency are apt for investigating the current issue pertaining to linear acceleration.

REFERENCES

Akanyeti, O., Putney, J., Yanagitsuru, Y. R., Lauder, G. V., Stewart, W. J., and Liao, J. C., "Accelerating fishes increase propulsive efficiency by modulating vortex ring geometry," Proc. Natl. Acad. Sci. U. S. A. **114**, 13828 (2017).

Alam, M. M. and Muhammad, Z., "Dynamics of flow around a pitching hydrofoil," J. Fluids Struct. **99**, 103151 (2020).

Ashraf, I., Bradshaw, H., Ha, T. T., Halloy, J., Godoy-Diana, R., and Thiria, B., "Simple phalanx pattern leads to energy saving in cohesive fish schooling," Proc. Natl. Acad. Sci. U. S. A. **114**, 9599 (2017).

Balay, S., Abhyankar, S., Adams, M. F., Benson, S., Brown, J., Brune, P., Buschelman, K., Constantinescu, E. M., Dalcin, L., Dener, A., Eijkhout, V., Faibussowitsch, J., Gropp, W. D., Hapla, V., Isaac, T., Jolivet, P., Karpeev, D., Kaushik, D., Knepley, M. G., Kong, F., Kruger, S., May, D. A., Curfman McInnes, L., Tran Mills, R., Mitchell, L., Munson, T., Roman, J. E., Rupp, K., Sanan, P., Sarich, J., Smith. B. F., Zampini, S., Zhang, H., Zhang, H., and Zhang, J., "PETSc web page," https://petsc.org/ (2023a).

Balay, S., Abhyankar, S., Adams, M. F., Benson, S., Brown, J., Brune, P., Buschelman, K., Constantinescu, E. M., Dalcin, L., Dener, A., Eijkhout, V., Faibussowitsch, J., Gropp, W. D., Hapla, V., Isaac, T., Jolivet, P., Karpeev, D., Kaushik, D., Knepley, M. G., Kong, F., Kruger, S., May, D. A., Curfman McInnes, L., Tran Mills, R., Mitchell, L., Munson, T., Roman, J. E., Rupp, K., Sanan, P., Sarich, J., Smith. B. F., Zampini, S., Zhang, H., Zhang, H., and Zhang, J., PETSc/TAO Users Manual, Argonne National Laboratory, ANL-21/39 - Revision 3.19 (2023b).

Balay, S., Gropp, W. D., McInnes, L. C., and Smith, B. F., "Efficient management of parallelism in object-oriented numerical software libraries," in *Modern Software Tools for Scientific Computing* (Birkhäuser, Boston, MA, 1997), available at https://link.springer.com/chapter/10.1007/978-1-4612-1986-6_8.

Bhalla, A. P. S., Bale, R., Griffith, B. E., and Patankar, N. A., "A unified mathematical framework and an adaptive numerical method for fluid-structure interaction with rigid, deforming, and elastic bodies," J. Comput. Phys. **250**, 446 (2013).

Bhalla, A. P. S., Bale, R., Griffith, B. E., and Patankar, N. A., "Fully resolved immersed electrohydrodynamics for particle motion, electrolocation, and self-propulsion," J. Comput. Phys. **256**, 88–108 (2014).

Bhalla, A. P. S., Griffith, B. E., and Patankar, N. A., "A forced damped oscillation framework for undulatory swimming provides new insights into how propulsion arises in active and passive swimming," PLoS Comput. Biol. **9**, e1003097 (2013).

Bhalla, A. P. S., Nangia, N., Dafnakis, P., Bracco, G., and Mattiazzo, G., "Simulating water-entry/exit problems using Eulerian–Lagrangian and fully-Eulerian fictitious domain methods within the open-source IBAMR library," Appl. Ocean Res. **94**, 101932 (2020).

Borazjani, I., "The functional role of caudal and anal/dorsal fins during the C-start of a bluegill sunfish," J. Exp. Biol. **216**, 1658–1669 (2013).

Borazjani, I. and Sotiropoulos, F., "Numerical investigation of the hydrodynamics of carangiform swimming in the transitional and inertial flow regimes," J. Exp. Biol. **211**, 1541 (2008).

Borazjani, I. and Sotiropoulos, F., "Numerical investigation of the hydrodynamics of anguilliform swimming in the transitional and inertial flow regimes," J. Exp. Biol. **212**, 576 (2009).

Borazjani, I. and Sotiropoulos, F., "On the role of form and kinematics on the hydrodynamics of self-propelled body/caudal fin swimming," J. Exp. Biol. **213**, 89 (2010).

Borazjani, I., Sotiropoulos, F., Tytell, E. D., and Lauder, G. V., "Hydrodynamics of the bluegill sunfish C-start escape response: Three-dimensional simulations and comparison with experimental data," J. Exp. Biol. **215**, 671 (2012).

Chao, L.-M., Alam, M. M., and Cheng, L., "Hydrodynamic performance of slender swimmer: Effect of travelling wavelength," J. Fluid Mech. **947**, A8 (2022).

Chao, L. M., Alam, M. M., and Ji, C., "Drag-thrust transition and wake structures of a pitching foil undergoing asymmetric oscillation," J. Fluids Struct. **103**, 103289 (2021).

Chao, L. M., Pan, G., Zhang, D., and Yan, G. X., "On the two staggered swimming fish," Chaos, Solitons Fractals **123**, 260 (2019).

Coombs, S. and Montgomery, J., "The role of flow and the lateral line in the multisensory guidance of orienting behaviors," in *Flow Sensing in Air and Water: Behavioral, Neural and Engineering Principles of Operation* (Springer, Berlin, Heidelberg, 2014), available at https://link.springer.com/chapter/10.1007/978-3-642-41446-6_3.

Cranmer, M., "Interpretable machine learning for science with PySR and SymbolicRegression.jl," arXiv:2305.01582 (2023).

Cranmer, M., Sanchez-Gonzalez, A., Battaglia, P., Xu, R., Cranmer, K., Spergel, D., and Ho, S., "Discovering symbolic models from deep learning with inductive biases," in *Advances in Neural Information Processing Systems* (MIT, 2020), Vol. 33.

Daghooghi, M. and Borazjani, I., "The hydrodynamic advantages of synchronized swimming in a rectangular pattern," Bioinspiration Biomimetics **10**, 056018 (2015).

Deng, J. and Liu, D., "Spontaneous response of a self-organized fish school to a predator," Bioinspiration Biomimetics **16**, 046013 (2021).

Deng, J., Shao, X. M., and Yu, Z. S., "Hydrodynamic studies on two traveling wavy foils in tandem arrangement," Phys. Fluids **19**, 113104 (2007).
Deng, J., Sun, L., Teng, L., Pan, D., and Shao, X., "The correlation between wake transition and propulsive efficiency of a flapping foil: A numerical study," Phys. Fluids **28**, 094101 (2016).
Deng, J., Teng, L., Pan, D., and Shao, X., "Inertial effects of the semi-passive flapping foil on its energy extraction efficiency," Phys. Fluids **27**, 053103 (2015).
Deng, J., Wang, S., Kandel, P., and Teng, L., "Effects of free surface on a flapping-foil based ocean current energy extractor," Renewable Energy **181**, 933 (2022).
Dewey, P. A., Quinn, D. B., Boschitsch, B. M., and Smits, A. J., "Propulsive performance of unsteady tandem hydrofoils in a side-by-side configuration," Phys. Fluids **26**, 041903 (2014).
Domenici, P. and Hale, M. E., "Escape responses of fish: A review of the diversity in motor control, kinematics and behaviour," J. Exp. Biol. **222**, jeb166009 (2019).
Dong, G. J. and Lu, X. Y., "Characteristics of flow over traveling wavy foils in a side-by-side arrangement," Phys. Fluids **19**, 057107 (2007).
Du Clos, K. T., Dabiri, J. O., Costello, J. H., Colin, S. P., Morgan, J. R., Fogerson, S. M., and Gemmell, B. J., "Thrust generation during steady swimming and acceleration from rest in anguilliform swimmers," J. Exp. Biol. **222**, jeb212464 (2019).
Eaton, R. C., Bombardieri, R. A., and Meyer, D. L., "The Mauthner-initiated startle response in teleost fish," J. Exp. Biol. **66**, 65 (1977).
Falgout, R., Cleary, A., Jones, J., Chow, E., Henson, V., Baldwin, C., Brown, P., Vassilevski, P., and Yang, U. M., *HYPRE: High Performance Preconditioners* (Lawrence Livermore National Laboratory, 2010).
Fish, F. E., "Advantages of aquatic animals as models for bio-inspired drones over present AUV technology," Bioinspiration Biomimetics **15**, 025001 (2020).
Floryan, D., Van Buren, T., Rowley, C. W., and Smits, A. J., "Scaling the propulsive performance of heaving and pitching foils," J. Fluid Mech. **822**, 386 (2017).
Gazzola, M., Argentina, M., and Mahadevan, L., "Scaling macroscopic aquatic locomotion," Nat. Phys. **10**, 758 (2014).
Gazzola, M., Mimeau, C., Tchieu, A. A., and Koumoutsakos, P., "Flow mediated interactions between two cylinders at finite Re numbers," Phys. Fluids **24**, 043103 (2012).
Griffith, B. E., see https://ibamr.github.io/about for "IBAMR: An Adaptive and Distributed-Memory Parallel Implementation of The Immersed Boundary Method" (2013).
Griffith, B. E. and Patankar, N. A., "Immersed methods for fluid-structure interaction," Annu. Rev. Fluid Mech. **52**, 421–448 (2020).
Grundner, A., Beucler, T., Gentine, P., and Eyring, V., "Data-driven equation discovery of a cloud cover parameterization," arXiv:2304.08063 (2023).
Gungor, A. and Hemmati, A., "The scaling and performance of side-by-side pitching hydrofoils," J. Fluids Struct. **104**, 103320 (2021).
Gungor, A., Khalid, M. S. U., and Hemmati, A., "Classification of vortex patterns of oscillating foils in side-by-side configurations," J. Fluid Mech. **951**, A37 (2022).
Gupta, S., Thekkethil, N., Agrawal, A., Hourigan, K., Thompson, M. C., and Sharma, A., "Body-caudal fin fish-inspired self-propulsion study on burst-and-coast and continuous swimming of a hydrofoil model," Phys. Fluids **33**, 091905 (2021).
Hornung, R. D. and Kohn, S. R., "Managing application complexity in the SAMRAI object-oriented framework," Concurrency Comput. **14**, 347 (2002).
Hornung, R. D., Wissink, A. M., and Kohn, S. R., "Managing complex data and geometry in parallel structured AMR applications," Eng. Comput. **22**, 181 (2006).
Huera-Huarte, F. J., "Propulsive performance of a pair of pitching foils in staggered configurations," J. Fluids Struct. **81**, 1–13 (2018).
Khalid, M. S. U., Wang, J., Akhtar, I., Dong, H., Liu, M., and Hemmati, A., "Why do anguilliform swimmers perform undulation with wavelengths shorter than their bodylengths?," Phys. Fluids **33**, 031911 (2021).
Khalid, M. S. U., Wang, J., Dong, H., and Liu, M., "Flow transitions and mapping for undulating swimmers," Phys. Rev. Fluids **5**, 063104 (2020).
Kirk, B. S., Peterson, J. W., Stogner, R. H., and Carey, G. F., "libMesh: A C++ library for parallel adaptive mesh refinement/coarsening simulations," Eng. Comput. **22**, 237 (2006).
Lamb, H., *Hydrodynamics*, 6th ed. (Cambridge University Press, Cambridge, 1932), p. 182.
Lecheval, V., Jiang, L., Tichit, P., Sire, C., Hemelrijk, C. K., and Theraulaz, G., "Social conformity and propagation of information in collective U-turns of fish schools," Proc. R. Soc. B **285**, 20180251 (2018).
Li, L., Liu, D., Deng, J., Lutz, M. J., and Xie, G., "Fish can save energy via proprioceptive sensing," Bioinspiration Biomimetics **16**, 056013 (2021a).
Li, L., Nagy, M., Graving, J. M., Bak-Coleman, J., Xie, G., and Couzin, I. D., "Vortex phase matching as a strategy for schooling in robots and in fish," Nat. Commun. **11**, 5408 (2020).
Li, L., Ravi, S., Xie, G., and Couzin, I. D., "Using a robotic platform to study the influence of relative tailbeat phase on the energetic costs of side-by-side swimming in fish," Proc. R. Soc. A **477**, 20200810 (2021b).
Li, Y., Wang, H., Li, Y., Ye, H., Zhang, Y., Yin, R., Jia, H., Hou, B., Wang, C., Ding, H. *et al.*, "Electron transfer rules of minerals under pressure informed by machine learning," Nat. Commun. **14**, 1815 (2023).
Lin, Z., Bhalla, A. P. S., Griffith, B. E., Sheng, Z., Li, H., Liang, D., and Zhang, Y., "How swimming style and schooling affect the hydrodynamics of two accelerating wavy hydrofoils," Ocean Eng. **268**, 113314 (2023a).
Lin, Z., Liang, D., and Zhao, M., "Numerical study of the interaction between two immersed cylinders," in The 12th International Conference on Hydrodynamics, 2016.
Lin, Z., Liang, D., and Zhao, M., "Interaction between two vibrating cylinders immersed in fluid," in *The 27th International Ocean and Polar Engineering Conference* (International Society of Offshore and Polar Engineers, San Francisco, California, 2017), p. 8.
Lin, Z., Liang, D., and Zhao, M., "Effects of damping on flow-mediated interaction between two cylinders," J. Fluids Eng. **140**, 091106 (2018a).
Lin, Z., Liang, D., and Zhao, M., "Flow-mediated interaction between a vibrating cylinder and an elastically-mounted cylinder," Ocean Eng. **158**, 389 (2018b).
Lin, Z., Liang, D., and Zhao, M., "Effects of Reynolds number on flow-mediated interaction between two cylinders," J. Eng. Mech. **145**, 04019104 (2019).
Lin, Z., Liang, D., and Zhao, M., "Flow-mediated interaction between a forced-oscillating cylinder and an elastically-mounted cylinder in less regular regimes," Phys. Fluids **35**, 013608 (2023b).
Lindsey, C. C., "Form, function, and locomotory habits in fish," in *Fish Physiology* (Academic Press, 1978), Vol. 7, available at https://books.google.com.sg/books?id=wnjnyAafAzUC&dq=Form,+function,+and+locomotory+habits+in+fish&lr=&hl=zh-CN&source=gbs_navlinks_s.
Ma, M., Huang, W. X., and Xu, C. X., "A dynamic wall model for large eddy simulation of turbulent flow over complex/moving boundaries based on the immersed boundary method," Phys. Fluids **31**, 115101 (2019).
Maertens, A. P., Gao, A., and Triantafyllou, M. S., "Optimal undulatory swimming for a single fish-like body and for a pair of interacting swimmers," J. Fluid Mech. **813**, 301 (2017).
Maertens, A. P., Triantafyllou, M. S., and Yue, D. K., "Efficiency of fish propulsion," Bioinspiration Biomimetics **10**, 046013 (2015).
Matchev, K. T., Matcheva, K., and Roman, A., "Analytical modeling of exoplanet transit spectroscopy with dimensional analysis and symbolic regression," Astrophys. J. **930**, 33 (2022).
Moriche, M., Flores, O., and García-Villalba, M., "Three-dimensional instabilities in the wake of a flapping wing at low Reynolds number," Int. J. Heat Fluid Flow **62**, 44 (2016).
Nair, S. and Kanso, E., "Hydrodynamically coupled rigid bodies," J. Fluid Mech. **592**, 393–411 (2007).
Nangia, N., Bale, R., Chen, N., Hanna, Y., and Patankar, N. A., "Optimal specific wavelength for maximum thrust production in undulatory propulsion," PLoS One **12**, e0179727 (2017a).
Nangia, N., Johansen, H., Patankar, N. A., and Bhalla, A. P. S., "A moving control volume approach to computing hydrodynamic forces and torques on immersed bodies," J. Comput. Phys. **347**, 437 (2017b).
Nangia, N., Patankar, N. A., and Bhalla, A. P. S., "A DLM immersed boundary method based wave-structure interaction solver for high density ratio multiphase flows," J. Comput. Phys. **398**, 108804 (2019).
Ni, J.-Y., Huang, W.-X., and Xu, C.-X., "Mode transition of a coupled rigid–flexible system in a uniform flow," Phys. Fluids **35**, 041706 (2023).

Pan, Y. and Dong, H., "Computational analysis of hydrodynamic interactions in a high-density fish school," Phys. Fluids **32**, 121901 (2020).
Pan, Y. and Dong, H., "Effects of phase difference on hydrodynamic interactions and wake patterns in high-density fish schools," Phys. Fluids **34**, 111902 (2022).
Partridge, B. L., "Internal dynamics and the interrelations of fish in schools," J. Comp. Physiol. **144**, 313 (1981).
Rosenthal, S. B., Twomey, C. R., Hartnett, A. T., Wu, H. S., and Couzin, I. D., "Revealing the hidden networks of interaction in mobile animal groups allows prediction of complex behavioral contagion," Proc. Natl. Acad. Sci. U. S. A. **112**, 4690 (2015).
Santo, V. D., Goerig, E., Wainwright, D. K., Akanyeti, O., Liao, J. C., Castro-Santos, T., and Lauder, G. V., "Convergence of undulatory swimming kinematics across a diversity of fishes," Proc. Natl. Acad. Sci. U. S. A. **118**, e2113206118 (2021).
Schwalbe, M. A., Boden, A. L., Wise, T. N., and Tytell, E. D., "Red muscle activity in bluegill sunfish *Lepomis macrochirus* during forward accelerations," Sci. Rep. **9**, 8088 (2019).
Sfakiotakis, M., Lane, D. M., and Davies, J. B. C., "Review of fish swimming modes for aquatic locomotion," IEEE J. Oceanic Eng. **24**, 237 (1999).
Shao, X., Pan, D., Deng, J., and Yu, Z., "Hydrodynamic performance of a fishlike undulating foil in the wake of a cylinder," Phys. Fluids **22**, 111903 (2010).
Shrivastava, M., Malushte, M., Agrawal, A., and Sharma, A., "CFD study on hydrodynamics of three fish-like undulating hydrofoils in side-by-side arrangement," in *Fluid Mechanics and Fluid Power—Contemprary Research* (Springer, 2016), available at https://link.springer.com/chapter/10.1007/978-81-322-2743-4_138.
Taylor, G. K., Nudds, R. L., and Thomas, A. L. R., "Flying and swimming animals cruise at a Strouhal number tuned for high power efficiency," Nature **425**, 707 (2003).
Thekkethil, N., Sharma, A., and Agrawal, A., "Unified hydrodynamics study for various types of fishes-like undulating rigid hydrofoil in a free stream flow," Phys. Fluids **30**, 077107 (2018).
Thekkethil, N., Sharma, A., and Agrawal, A., "Self-propulsion of fishes-like undulating hydrofoil: A unified kinematics based unsteady hydrodynamics study," J. Fluids Struct. **93**, 102875 (2020).
Thekkethil, N., Shrivastava, M., Agrawal, A., and Sharma, A., "Effect of wavelength of fish-like undulation of a hydrofoil in a free-stream flow," Sādhanā **42**, 585 (2017).
Triantafyllou, M. S., Triantafyllou, G. S., and Gopalkrishnan, R., "Wake mechanics for thrust generation in oscillating foils," Phys. Fluids A **3**, 2835 (1991).
Triantafyllou, M. S., Weymouth, G. D., and Miao, J., "Biomimetic survival hydrodynamics and flow sensing," Annu. Rev. Fluid Mech. **48**, 1–24 (2016).
Tytell, E. D., "Kinematics and hydrodynamics of linear acceleration in eels, *Anguilla rostrata*," Proc. R Soc. B **271**, 2535 (2004).
Tytell, E. D. and Lauder, G. V., "Hydrodynamics of the escape response in bluegill sunfish, *Lepomis macrochirus*," J. Exp. Biol. **211**, 3359 (2008).
Van Buren, T., Floryan, D., Quinn, D., and Smits, A. J., "Nonsinusoidal gaits for unsteady propulsion," Phys. Rev. Fluids **2**, 053101 (2017).
Wang, L. H., Xu, C. X., Sung, H. J., and Huang, W. X., "Wall-attached structures over a traveling wavy boundary: Turbulent velocity fluctuations," Phys. Rev. Fluids **6**, 034611 (2021).
Webb, P. W., "Form and function in fish swimming," Sci. Am. **251**, 72 (1984).
Wei, C., Hu, Q., Zhang, T., and Zeng, Y., "Passive hydrodynamic interactions in minimal fish schools," Ocean Eng. **247**, 110574 (2022).
Weihs, D., "Hydromechanics of fish schooling," Nature **241**, 290–291 (1973).
Yu, Y.-L. and Huang, K.-J., "Scaling law of fish undulatory propulsion," Phys. Fluids **33**, 061905 (2021).
Yucel, S. B., Sahin, M., and Unal, M. F., "Propulsive performance of plunging airfoils in biplane configuration," Phys. Fluids **34**, 033611 (2022).
Zheng, M., Kashimori, Y., Hoshino, O., Fujita, K., and Kambara, T., "Behavior pattern (innate action) of individuals in fish schools generating efficient collective evasion from predation," J. Theor. Biol. **235**, 153 (2005).